CHEMISTRY OF MATERIALS

Open Access

pubs.acs.org/cm

Article

Alumina Priming-Mediated Enhanced Binding of Diethylzinc with Carbonyl Groups in Poly(Methyl Methacrylate) during Vapor-Phase Infiltration

Nikhil Tiwale,* Ashwanth Subramanian, Sayantani Sikder, Xiaohui Qu,* Guillaume Freychet, Eliot Gann, Cherno Jaye, Kim Kisslinger, Jorge Anibal Boscoboinik, and Chang-Yong Nam*

Cite This: *Chem. Mater.* 2026, 38, 1751−1765

Read Online

ACCESS | Metrics & More | Article Recommendations | Supporting Information

ABSTRACT: Vapor-phase infiltration (VPI) of inorganic materials in polymers is increasingly becoming popular for synthesizing various functional hybrid materials. While AlO_x infiltration using trimethylaluminum (TMA) has been extensively studied, the mechanism of diethylzinc (DEZ)-based ZnO_x infiltration, especially one that is initiated by AlO_x priming, has not received much attention because highly reactive hydroxyl groups generated by AlO_x-priming are expected to dominate the initial binding of DEZ, thus enabling the overall ZnO_x VPI. Here, we interrogate the ZnO_x infiltration mechanism in AlO_x-primed poly(methyl methacrylate) (PMMA) in comparison to the control AlO_x-only infiltration by utilizing a suite of complementary characterizations, including quartz crystal microbalance mass gain measurement, transmission electron microscopy, infrared reflection−absorption spectroscopy (IRRAS), and synchrotron X-ray absorption spectroscopy (XAS). The multivalent TMA precursor and associated hyperbranched AlO_x network can quickly saturate the AlO_x infiltration by clogging the polymer-free volume near the top. On the contrary, the ZnO_x infiltration using divalent DEZ precursor, once activated via AlO_x-priming, can lead to accelerated ZnO_x infiltration. With the help of IRRAS, XAS, and density functional theory (DFT) simulations, we uncover that the AlO_x-priming enhances the reactivity of neighboring carbonyl groups toward DEZ and opens up simultaneous reaction pathways, leading to accelerated high-fidelity infiltration of ZnO_x.

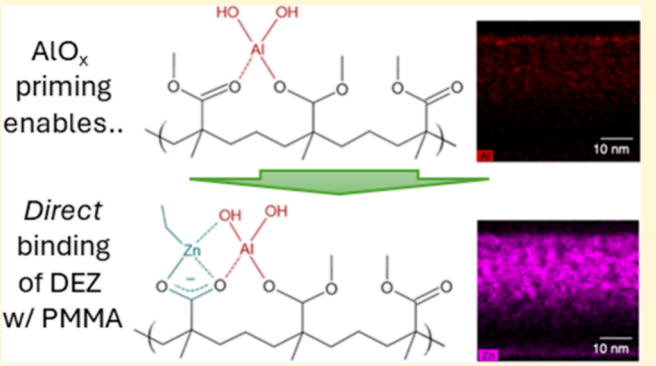

INTRODUCTION

As a scalable material hybridization technique, vapor-phase infiltration (VPI) synthesis has increasingly attracted widespread interest over the past decade.[1−4] VPI has shown considerable impact on the applications critical to semiconductor fabrication and processing, such as ex-situ synthesis of hybrid resists for advanced lithography,[5−9] enhanced dry-etch pattern transfer performance,[6,10−12] doping organic semiconductors,[13−15] direct-write patterning of functional materials for electronic,[16−20] optoelectronic,[21,22] and sensing devices.[17,23] The applications of this technique have also expanded to a variety of areas, including chemical separation/filtration membranes,[24−27] and enhanced mechanical properties.[28−31] A wide range of characterization techniques, such as quartz crystal microbalance (QCM),[6,32,33] spectroscopic ellipsometry (SE),[34,35] cross-sectional transmission electron microscopy (TEM)[6−8] coupled with energy-dispersive X-ray spectroscopy (EDS),[8,9,31,36] Fourier transform infrared spectroscopy (FTIR),[37,38] have been implemented over the years to gain an understanding of the underlying physicochemical processes.

In a typical VPI process, the organometallic precursors diffuse into the polymer matrix and bind to reactive functional groups, forming molecular metal oxide species inside the bulk polymer bulk volume. For example, during alumina infiltration into poly(methyl methacrylate) (PMMA), the Lewis acidic aluminum precursor, trimethylaluminum (TMA), forms a Lewis adduct with the Lewis-basic carbonyl group in PMMA. Subsequently, water is diffused into the PMMA matrix, converting the carbonyl-TMA adduct into AlO_x/Al−OH species.[3,4,37] The presence of these hydroxyl groups exhibits a higher reactivity toward the incoming metal precursor, thus becoming a preferential location for subsequent metal oxide growth. This enhanced reactivity after the first alumina cycle can be exploited to enable infiltration of various less reactive

Received: September 29, 2025
Revised: December 6, 2025
Accepted: December 10, 2025
Published: February 3, 2026

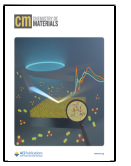

metal precursors (i.e., alumina priming), which can react directly with hydroxyl groups rather than with the polymer's inherent functional groups.[39−42]

For instance, the VPI of ZnO, which can provide many functional applications due to its semiconducting properties,[43−46] typically relies on diethylzinc (DEZ) as a Zn precursor, but it is a weaker Lewis acid compared to TMA, thus not readily reacting with the carbonyl group in PMMA. Peng et al. demonstrated that by enhancing the reactivity of the PMMA matrix via alumina priming, DEZ molecules can be made to infiltrate and then be converted to ZnO_x.[39] Ocola et al. further investigated this route using photoluminescence (PL), Raman scattering, X-ray photoelectron spectroscopy (XPS), and extended X-ray absorption fine structure (EXAFS).[41] Key findings of the study included the dramatic PL intensity change from the second to the third infiltration cycle, and the resulting ZnO_x exhibits a diffused/distorted structure compared to wurtzite crystalline ZnO. Collectively, these studies implicated AlO_x-generated hydroxyls as the principal sites with which infiltrating DEZ reacts.

Despite these advances, the mechanistic basis of alumina priming—particularly its influence on infiltration depth, surface clogging, and whether growth is reaction- or diffusion-limited—remains poorly understood. In addition, precursor-delivery conditions (static vs dynamic, conventional vs microdose) can significantly shape local reaction environments and transport, potentially altering infiltration pathways and products.

In this study, we investigate how hydroxyl- and carbonyl-mediated processes govern metal oxide network growth within PMMA matrix during multicycle VPI. Motivated by our interest in the application of VPI on generating organic−inorganic hybrid photoresist materials,[5−9] we focus on ultrathin (~25−30 nm) PMMA films and employ non-equilibrium infiltration protocols to achieve precise cycle-by-cycle control. Through a combination of in situ QCM mass gain monitoring, cross-sectional scanning TEM (STEM), infrared reflection−absorption spectroscopy (IRRAS), and near-edge X-ray absorption fine structure (NEXAFS) spectroscopy supported by density functional theory (DFT) simulations, we uncover two unexpected behaviors: (1) alumina infiltration rapidly plateaus because branched network formation clogs the near-surface, limiting penetration; and (2) although DEZ requires AlO_x priming to initiate, subsequent ZnO_x cycles exhibit increasing mass uptake and progressively deeper, more uniform infiltration. IRRAS, NEXAFS and DFT analyses reveal that enhanced carbonyl reactivity adjacent to alumina adducts underlies this improved ZnO_x VPI fidelity—a mechanistic insight into how AlO_x priming can enhance the intrinsic reactivity of chemical moieties already available within the polymer matrix, in this case, the carbonyl group in PMMA, in addition to generating reactive hydroxyl groups, enabling infiltration of weakly reactive organometallic precursors during VPI.

RESULTS AND DISCUSSION

Due to insufficient reactivity between the PMMA matrix and the DEZ precursor, alumina priming is a popular route for ZnO_x infiltration into PMMA.[39−42] Figure 1a depicts a high-resolution cross-sectional TEM micrograph acquired from PMMA infiltrated with AlO_x-primed ZnO_x when a static 60 s DEZ/H_2O exposure was used during respective half-cycles, and a total of 10 infiltration cycles were carried out (note: all

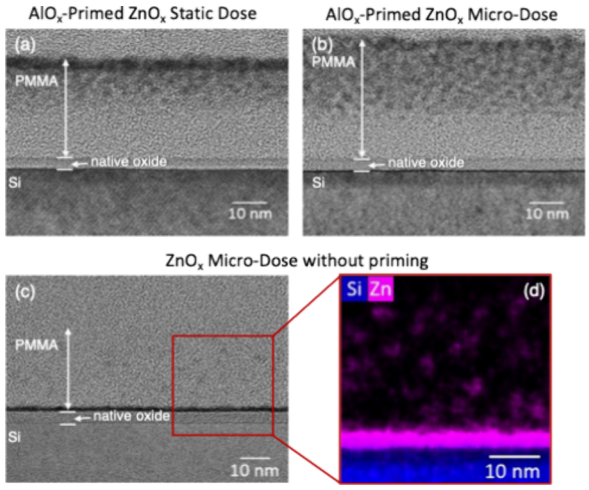

Figure 1. High-resolution cross-section TEM micrographs of (a) AlO_x-primed ZnO_x infiltration with static dosing of DEZ/H_2O showing a gradient of infiltrated species; (b) AlO_x-primed ZnO_x infiltration when microdosing protocol is used for DEZ/H_2O showing uniform distribution of infiltrated species; and (c) ZnO_x infiltration using microdosing protocol without priming step showing no discernible infiltration except for some ZnO granules formed by kinetic trapping of precursors and deposition of ZnO_x on the PMMA-SiO_2 interface. (d) Zoomed-in EDS elemental mapping of (c) confirming the granules and interface deposition of ZnO_x. Note that the samples (only in this figure) used starting PMMA films of ~50 nm formed using PMMA 950 A2 directly.

VPI experiments were conducted at 85 °C in this study; see Experimental Methodologies). Key aspects that can be clearly seen are shallow infiltration depth, nonuniform (gradient) infiltration profile, and dense, clogged ZnO_x layer at the top. When the precursor exposure for DEZ/H_2O was changed to the microdose protocol (6 precursor pulses at 10 s intervals), not only was the film swelling higher, with almost twice the infiltration depth, but also a more uniform infiltration profile was seen with the less dense top layer (Figure 1b). In order to clarify the role played by alumina priming and explore the possibility of kinetic physical trapping mediated ZnO_x infiltration, the same microdose protocol was repeated without the alumina priming. As shown in Figure 1c,d, sporadic kinetic trapping of ZnO_x granules was observed, albeit only in a tiny amount. What was more noteworthy was the formation of a dense ZnO_x layer at the bottom interface of the PMMA film. Such growth can be attributed to the weakly reactive DEZ/H_2O molecules having been able to diffuse all the way through the thin PMMA film unreacted and depositing at the reactive interface offered by the native SiO_x surface of the substrate.[9,19] These observations clarify two crucial factors: the necessity of alumina priming to boost the chemical reactivity of the DEZ precursor with the polymer matrix and the ability to overcome limited precursor diffusion into the polymer matrix by using a dynamic microdose protocol instead of static precursor dosing.

In order to gain deeper insights into the evolution of infiltration synthesis over multiple cycles, in situ mass uptake of AlO_x and AlO_x-primed ZnO_x infiltration processes was monitored and extracted using standard QCM measurements (Figure 2a,b). Both figures consist of two correlated transient plots—the top plot depicts the evolution of QCM mass added, and the bottom plot depicts the evolution of chamber pressure. The beginning of each infiltration cycle is marked on the top axis of the mass gain subplot. Each precursor half-cycle is

https://doi.org/10.1021/acs.chemmater.5c02584
Chem. Mater. 2026, 38, 1751−1765

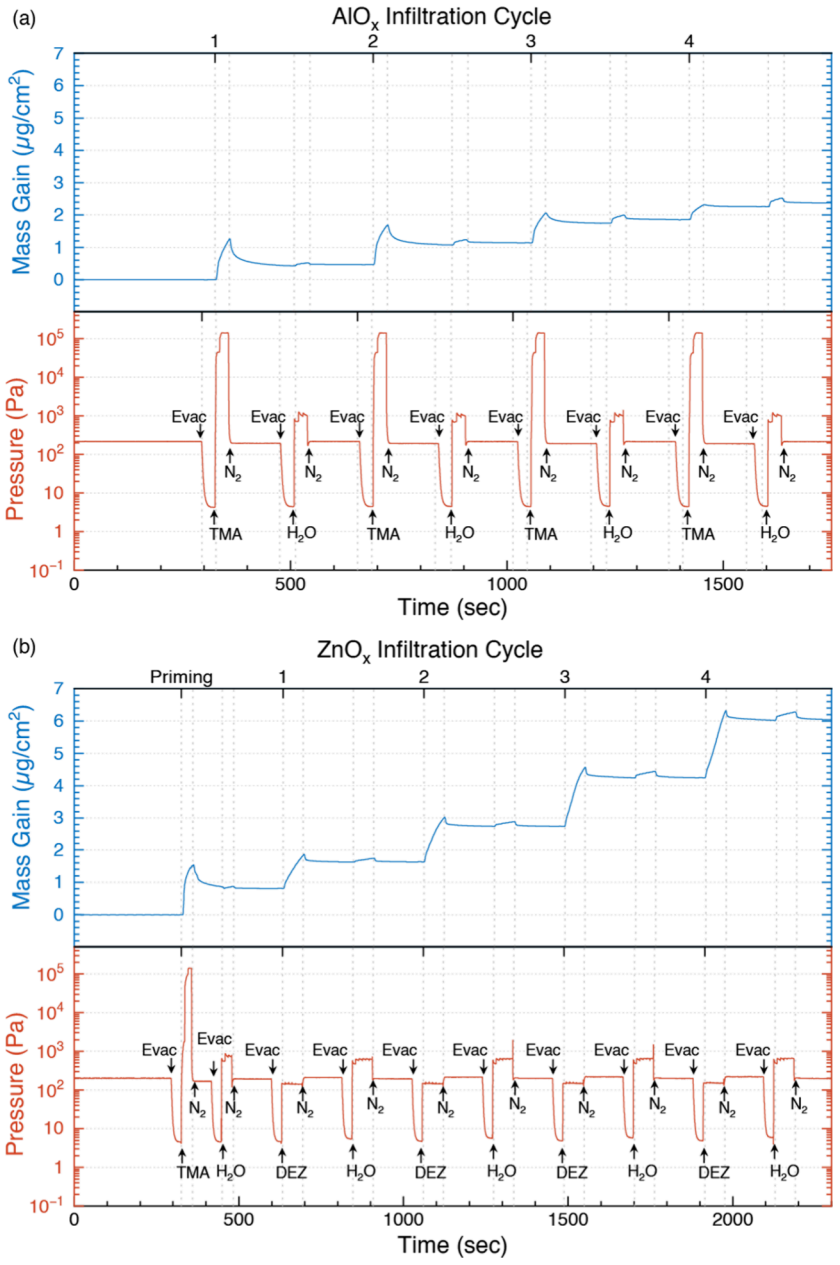

Figure 2. QCM mass gain per unit area over 4 cycles of (a) AlO_x and (b) AlO_x-primed ZnO_x infiltration into PMMA thin film.

preceded by a 30 s chamber evacuation where pressure drops down to ∼4 Pa. After the prescribed period of precursor exposure, the pressure changes to ∼267 Pa corresponding to a chamber purge under 10^{-4} m^3/min (100 sccm) N_2 flow. In the pressure variation plot for AlO_x infiltration, the most significant pressure value corresponds to 30 s TMA exposure half-cycle (∼1×10^5 Pa; inflated reading by a Pirani gauge under TMA), whereas the pressure during the 30 s water exposure half-cycle was smaller (∼933−1066 Pa). In the pressure variation plot of AlO_x-primed ZnO_x infiltration, the 30 s priming step has a similar considerable pressure of TMA followed by 30 s of water exposure (∼933−1066 Pa). Subsequently, during the 60 s DEZ exposure steps, the chamber pressure is ∼1×10^2 Pa, which is even lower than the pressure during the purge step (∼267 Pa).

During the first TMA exposure half-cycle, the diffusion of TMA into the PMMA film increased the QCM mass by 1.26 $\mu g/cm^2$; however, it dropped to 0.42 $\mu g/cm^2$ (33.5%) after the purge step. This observation can be attributed to the fact that during TMA exposure, not all TMA molecules form chemically bonded Al-adducts with PMMA carbonyl groups.[37] As shown in Scheme 1a, some TMA molecules form weakly bonded Al-adducts with one or more carbonyl groups. Once the chamber purge begins, these weakly bonded Al-adducts lose their binding to the PMMA matrix and diffuse out of the thin film, leaving behind only chemically bound Al-adducts in the PMMA matrix (Scheme 1b) and resulting in a drop in the QCM mass. Subsequently, during the water exposure half-cycle, only a small mass gain was seen (due to the smaller molecular weight of the water molecule). The methyl groups in chemically bonded Al-adducts are oxidized to hydroxyl groups (Scheme 1c), corresponding to a small QCM mass gain of up to 0.47 $\mu g/cm^2$ at the end of the first infiltration cycle. During the subsequent infiltration cycles, a decreasing amount of mass

https://doi.org/10.1021/acs.chemmater.5c02584
Chem. Mater. 2026, 38, 1751−1765

Scheme 1. (a) Section of Five Methacrylate Groups from PMMA Chain; (b) Formation of Different Adducts during the TMA Exposure Phase—Some TMA Chemically Bonded to Carbonyl Oxygen Leading to the Formation of −O−Al−CH_3 Species, Some TMA Only Forming Electrostatic Interactions with One or More Carbonyls; (c) after the Purging Step, Mostly Only the Chemically Bonded TMA Remains within Polymer Matrix; (d) Once Subjected to Water, the Hydrolysis Leads to Formation of −O−Al(OH)$_2$ Species at the Infiltration Sites

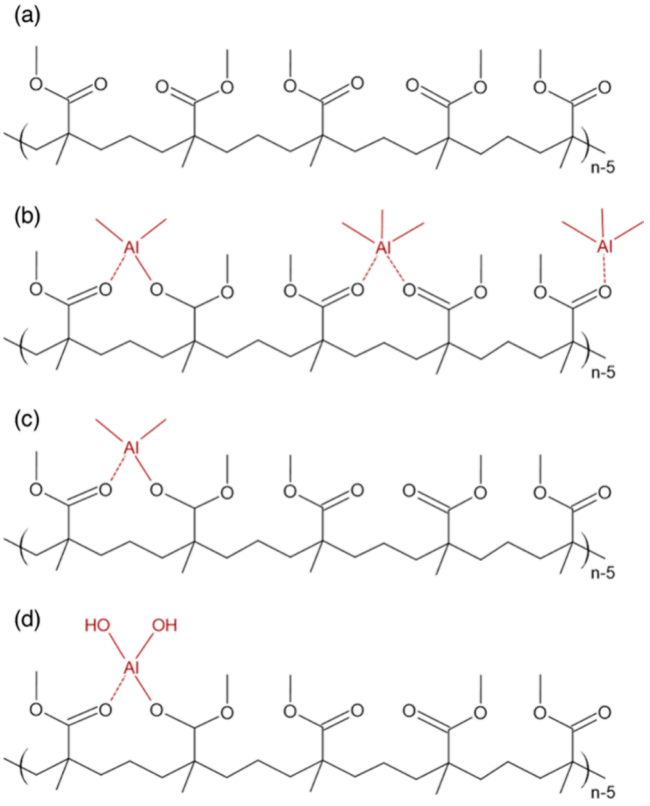

gain is seen during the TMA exposure half-cycle (1.23, 0.93, and 0.46 $\mu g/cm^2$ for the second, third, and fourth cycles, respectively), suggesting a lesser amount of TMA sorption into the PMMA matrix. Clogging of the free polymer volume as a result of AlO_x infiltration could be the cause of TMA sorption being hindered.

Interestingly, an increasing fraction of this TMA is retained after the purge step (49.4, 65.9, and 86.5% for the second, third, and fourth cycles, respectively), indicating that a larger degree of chemically bound adduct is formed. This can be attributed to the fact that after the first infiltration cycle, along with carbonyl groups, the PMMA matrix also contains −Al−OH groups (Scheme 1c), which are chemically more reactive toward TMA molecules. In fact, a greater number of hydroxyl groups per carbonyl are generated every cycle (Scheme 2), and the infiltration is increasingly mediated through hydroxyl groups instead of binding with carbonyl groups. During the fourth infiltration cycle, most of the TMA diffused into the PMMA is retained, although a smaller amount of TMA was diffused initially.

In the case of AlO_x-primed ZnO_x infiltration, the priming step showed behavior similar to that of the first AlO_x infiltration cycle, except that a static 30 s dose was used during priming and a shorter purge step was used between

Scheme 2. AlO_x Infiltration over 1−4 Cycles into the Top Layers of PMMA Leads to Clogging of the Free Volume[a]

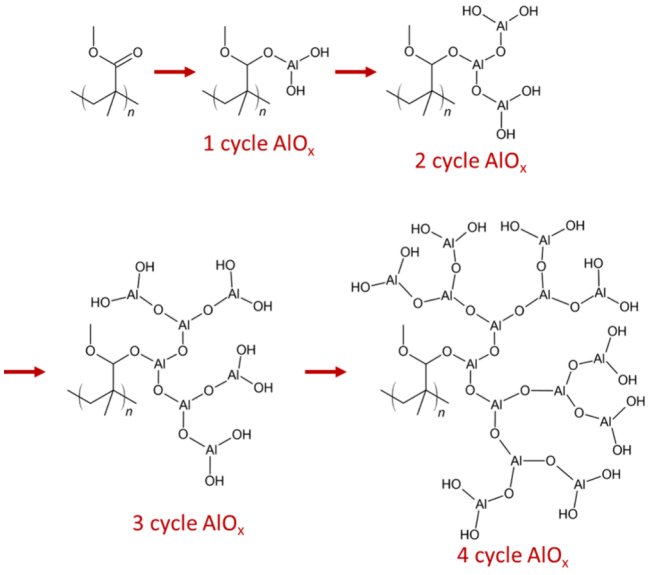

[a]After the hydroxyl groups are formed during the priming cycle, TMA molecules react with these hydroxyl groups and subsequently get hydrolyzed themselves to form twice the number of hydroxyl groups every cycle. This leads to a hyperbranched AlO_x network within a few cycles and clogs the free volume.

TMA and water half-cycles. Thus, 0.81 $\mu g/cm^2$ AlO_x was infiltrated during the priming step. During the first DEZ half-cycle, which consisted of 60 s of microdose exposure, a QCM mass uptake of 1.05 $\mu g/cm^2$ was observed. Considering the fact that the DEZ is much heavier than TMA, it should be noted that, in fact, the sorption of a smaller number of DEZ molecules into the PMMA matrix took place. As opposed to TMA, however, most of these DEZ molecules were retained through the purge step, changing the QCM mass uptake from 1.05 to 0.81 $\mu g/cm^2$ (77.4% retained). Considering the conventional understanding of the priming-initiated infiltration, the hydroxyl groups formed during priming cycles are chemically more reactive than the carbonyl groups inherently present in PMMA. Therefore, although DEZ molecules do not bind to the carbonyl oxygen of the pristine PMMA matrix themselves, they do bind with hydroxyl groups generated by the priming cycle. Thus, infiltration takes place via hydroxyl mediation. As per the hydroxyl-mediated infiltration pathway, due to the bivalency of the Zn atom, at the end of each cycle, the same number of hydroxyl groups get generated as were available for reacting to DEZ at the beginning of the cycle, forming a linear ZnO_x network as shown in Scheme 3. It should be noted that the linear chain formation is a rather simplistic depiction, and it is likely that instead the ZnO_x starts to form 2D or 3D clusters. For such linear growth, an equal amount of mass gain and retention would be expected from cycle to cycle. Interestingly, during the second, third, and fourth cycles, an increasing amount of DEZ mass gain is seen (1.41, 1.83, and 2.08 $\mu g/cm^2$, respectively), and at the same time, an increasing fraction of this DEZ is retained through the purge steps (79.4, 81.9, and 85.3%, respectively). The linear growth depicted in Scheme 3 by itself cannot result in an increasing mass gain from cycle to cycle. In order to exhibit an increasing mass gain cycle to cycle, an additional mechanism different from Scheme 3 should also be in the works, and

https://doi.org/10.1021/acs.chemmater.5c02584
Chem. Mater. 2026, 38, 1751−1765

Scheme 3. Conventionally Expected Progression of AlO_x-Primed ZnO_x Infiltration into PMMA Matrix over (1−4) Cycles[a]

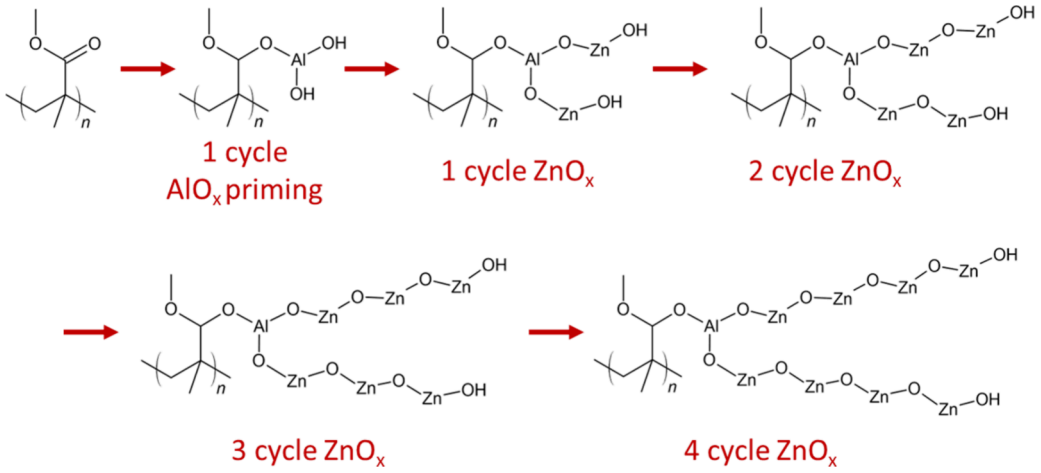

[a]After the hydroxyl groups are formed during the priming cycle, the DEZ molecules are considered to be reacting to these hydroxyl groups and subsequently getting hydrolyzed themselves to form new hydroxyl groups. This linear growth progression continues over multiple cycles.

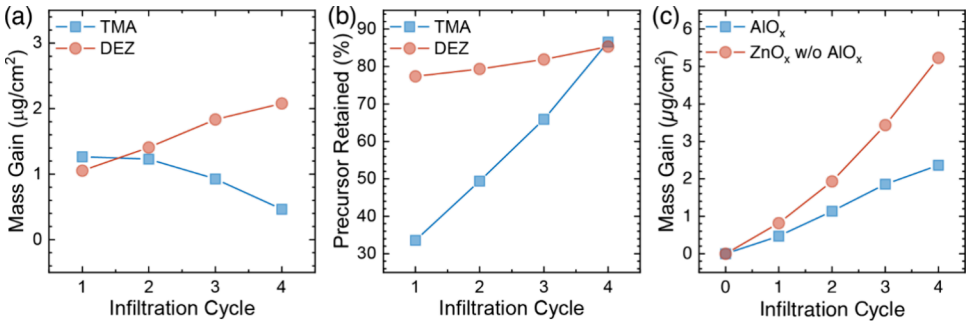

Figure 3. (a) Precursor mass gained during the metal precursor exposure half-cycle. (b) Percentage of precursor mass retained after the N_2 purge and chamber evacuation phase. (c) Estimated mass gain of AlO_x and ZnO_x at the end of each infiltration cycle (note that for the ZnO_x infiltration, only ZnO_x mass gain is depicted by subtracting the AlO_x mass gain of the priming cycle).

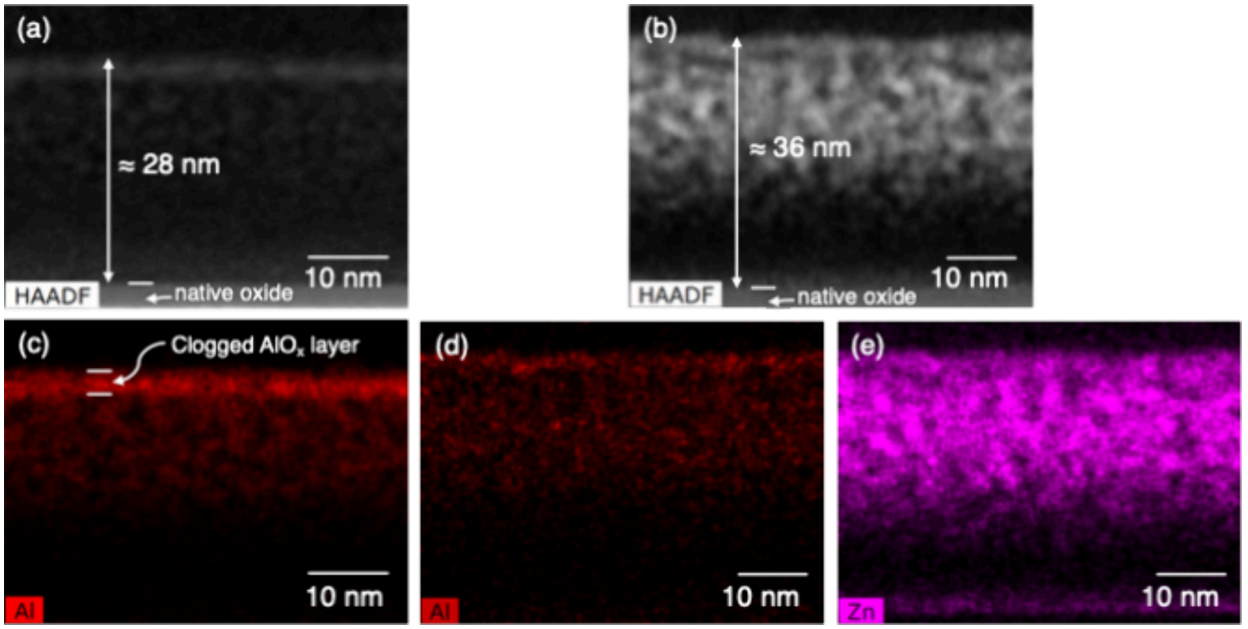

Figure 4. Cross-section HAADF images of PMMA thin film infiltrated with (a) 4-cycle AlO_x and (b) AlO_x-primed 4-cycle ZnO_x. The latter shows larger swelling (~36 nm) compared to the former (~28 nm). EDS elemental mapping depicting (c) Al in AlO_x-infiltrated PMMA, along with (d) Al and (e) Zn in AlO_x-primed-ZnO_x-infiltrated PMMA. A clogged AlO_x layer is clearly visible in AlO_x infiltration, while such a clogged layer is absent in ZnO_x infiltration.

https://doi.org/10.1021/acs.chemmater.5c02584
Chem. Mater. 2026, 38, 1751−1765

perhaps the matrix might become chemically more reactive toward incoming DEZ molecules as the ZnO_x infiltration proceeds. This will be further investigated in a subsequent section.

The observations from the transient mass gain measurements are summarized in Figure 3. The mass gain during the first cycle is almost the same for both AlO_x and ZnO_x infiltration. However, a decreasing amount of mass gain is observed cycle to cycle during the TMA exposure step of AlO_x infiltration. In contrast, an increasing amount of mass gain is seen cycle to cycle for DEZ during AlO_x-primed ZnO_x infiltration (Figure 3a). Of the precursor mass gain during the exposure cycle, the precursor fraction retained from cycle to cycle is also shown in Figure 3b. Although only ∼33% TMA is retained during the first cycle, the retention increases to above 85% for the fourth AlO_x infiltration cycle. However, in the case of AlO_x-primed ZnO_x infiltration, the initial ∼77% of DEZ retention shows a slight increase through cycles 2−4, reaching ∼85%. As a complete effect of precursor sorption and retention, the mass gain per unit area at the end of each full cycle was also estimated from transient mass gain plots, and the evolution is depicted in Figure 3c. It should be noted that ZnO_x molecules are heavier than AlO_x, and the mass gain after the priming cycle was subtracted from the total mass gain to estimate the mass gain of ZnO_x only. It is evident that the AlO_x mass gain is not only slower than the ZnO_x but also seems to be plateauing. ZnO_x mass gain, on the other hand, appears to be accelerating instead.

Evidence of Diminishing AlO_x Infiltration Due to Top-Layer Clogging

We utilized STEM to take a closer look at the cross sections of the PMMA films after four infiltration cycles of both AlO_x and AlO_x-primed ZnO_x. The high-angle annular dark-field (HAADF) images, along with EDS elemental mapping, are presented in Figure 4. While only a small amount of thickness swelling is observed for the AlO_x-infiltrated film, the AlO_x-primed-ZnO_x-infiltrated film is almost 25% more swollen, indicating a greater amount of material incorporation. Moreover, a dense, clogged alumina layer is apparent in the EDS elemental mapping of the AlO_x-infiltrated sample. In contrast, no such layer is seen in the AlO_x-primed-ZnO_x-infiltrated film. The formation of such a clogged-up layer likely hinders the sorption of new TMA molecules in successive cycles, leading to a smaller TMA mass gain (Figure 3a) as compared to DEZ. Interestingly, in the EDS elemental mapping of Zn in Figure 4e, discernible ZnO_x deposition can be seen at the substrate native oxide interface. As we explained earlier, unreacted DEZ/H_2O can diffuse through the entirety of the thin PMMA film due to their low reactivity with the polymer matrix and react with the native oxide at the substrate interface, resulting in ZnO_x deposition. This also sheds light on the fact that, albeit accelerated by priming, ZnO_x infiltration remains reaction-limited and not diffusion-limited.

As depicted in Scheme 2, during the first infiltration cycle, the carbonyl group of PMMA reacts with the TMA precursor, and the adduct thus formed is subsequently hydrolyzed by water. From the second cycle onward, however, the prevalence of highly reactive −Al−OH species inside PMMA preferentially binds with incoming TMA molecules. Notably, the number of −OH groups doubles during each cycle, making them available to react in subsequent cycles. This results in the possibility of twice as many TMA molecules binding to the matrix in each infiltration cycle compared with the previous cycle. Consequently, a dense AlO_x network can be rapidly formed, and the polymer-free volume near the film's top surface can quickly become clogged, leading to saturation of the mass gain. It should be noted that Schemes 1 and 2 and the above discussion assume the interaction of a single TMA molecule, but in reality, TMA molecules are known to dimerize below 100 °C.[47,48] Thus, at our applied VPI temperature (85 °C), TMA molecules are expected to exist as dimers. The two bridging C atoms in the dimer are ionic in nature compared to the terminal C atoms.[49] The highly negative partial charge on the bridging atoms renders them highly reactive as a methyl nucleophile; therefore, they should be capable of initiating a Lewis adduction reaction, which could otherwise be challenging to occur. The formation of dimers, and hence the carbanionic bridging methyl group, leads to increased reactivity of TMA toward PMMA. This unique feature is crucial in the formation of chemically bonded, stable infiltration products. The reaction with water molecules during the oxidation half-cycle also likely starts with the bridging carbon atom.[50] However, an uncontrolled hydrolysis process can lead to the formation of large methyl-aluminoxane clusters or even aluminum oxide blocks,[31] which would render the hyperbranched AlO_x network resulting via hydroxyl-mediated infiltration (Scheme 2) and the subsequent clogging of polymer-free volume even more significant. During AlO_x-primed ZnO_x infiltration (Scheme 3), carbonyl groups are converted to −Al−OH species during the priming cycle. However, during the subsequent ZnO_x infiltration cycles, the number of available −OH groups remains the same as the previous cycle in principle due to the linearity of the DEZ molecule in contrast to the −OH group proliferation scenario of AlO_x infiltration. As a result, the same number of Zn atoms is added in each cycle via hydroxyl-mediated infiltration. Thus, the polymeric-free volume does not get clogged up as quickly, and a nearly monotonic mass gain is sustained.

Anomalous Observations in NEXAFS Spectroscopy

The evolution of the chemical species during the infiltration cycles was investigated by using NEXAFS spectroscopy. NEXAFS is an effective technique to probe specific chemical bonds in near-surface regions of the material (the signal is exponential, with a decay length of ∼3 nm depending on the material and the grid bias).[51] The technique relies upon the excitation of core-level electrons of an element directly to a free state or to bound empty and partially occupied states. These states can, through various decay processes, result in either a high-energy Auger electron or the emission of a fluorescent X-ray. Electrons have a short escape depth; therefore, those measured in a partial electron yield (PEY) experiment must originate from very close to the surface, whereas fluorescent X-rays can travel much further. The technique is increasingly being used for the investigation of a new generation of extreme ultraviolet (EUV) photoresists, such as sol−gel-based glassy metal-silicate-hybrid resists[52] and oxo-cluster resists.[53]

The NEXAFS measurements were carried out at both the carbon K-edge and oxygen K-edge, and the extracted spectra were normalized for the tail region far away from the photon energy corresponding to the specific elemental edge. The PEY spectra for both AlO_x and AlO_x-primed-ZnO_x-infiltrated PMMA samples are shown in Figure 5, and specific peaks corresponding to various electronic transitions are assigned

https://doi.org/10.1021/acs.chemmater.5c02584
Chem. Mater. 2026, 38, 1751−1765

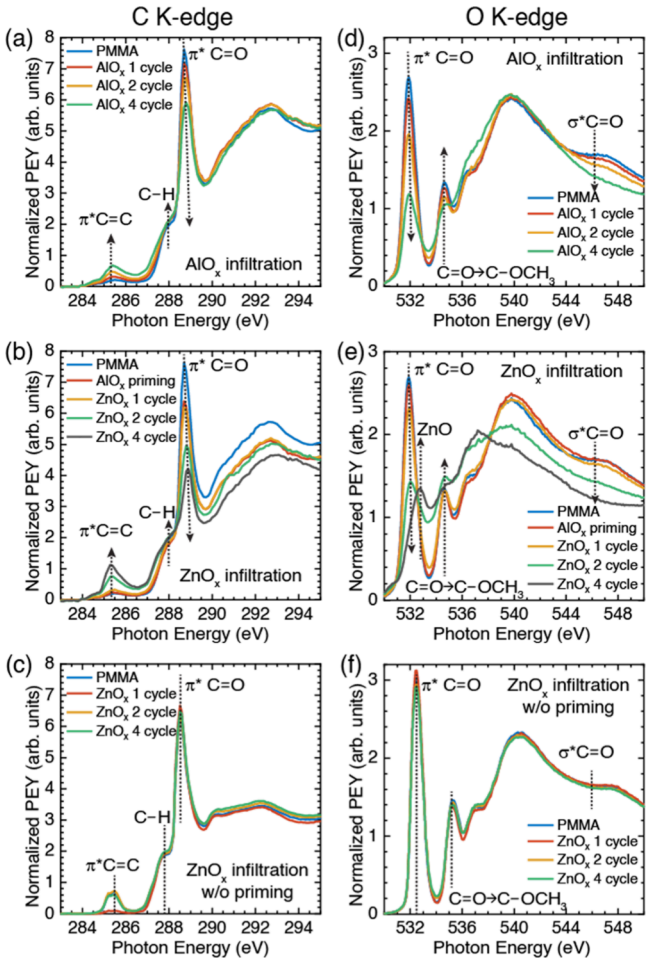

Figure 5. NEXAFS spectra obtained at carbon K-edge (a–c) and oxygen K-edge (d–f) for AlO_x infiltration (a,d), AlO_x-primed-ZnO_x infiltration (b,e), and ZnO_x infiltration without priming (c,f), respectively. The peak corresponding to the 1s → π^* C═O transition in both carbon and oxygen spectra decreases with an increasing number of infiltration cycles for both AlO_x and AlO_x-primed ZnO_x infiltration. However, no substantial change in the corresponding peak could be seen for ZnO_x infiltration without priming, suggesting negligible infiltration.

based on prior literature (Tables 1 and 2). The most prominent peak in carbon K-edge spectra (Figure 5a,b) at

Table 1. Peak Assignment for Carbon K-Edge

energy (eV)	assignment	refs
285	C 1s → $\pi^*_{C=C}$	54
288	C 1s C–H → π^*_{C-H}	58
289.5	C 1s → $\pi^*_{C=O}$	58
292	C 1s → $\sigma^*_{C-C,\ C-O}$	58
296	C 1s → $\sigma^*_{C=O}$	58

289.5 eV corresponds to C 1s → $\pi^*_{C=O}$. While both AlO_x and AlO_x-primed-ZnO_x infiltration samples exhibit a decrease in the intensity of this peak with an increasing number of infiltration cycles, the peak intensity variation per cycle is larger for AlO_x-primed-ZnO_x infiltration (with a slight shift toward higher energy) compared to AlO_x infiltration. The peak at 285 eV was attributed to the C 1s → $\pi^*_{C=C}$ transition.[54] However, it may also originate from graphitic carbon formed by X-ray

Table 2. Peak Assignment for Oxygen K-Edge

energy (eV)	assignment	refs
531.5	O 1s → $\pi^*_{C=O}$	55
532.5	ZnO O 1s → 2p–Zn 3d4s	56,57
534.5	O 1s (O–CH_3) → $\pi^*_{C=O}$ &O 1s (C═O) → $\sigma^*_{C\text{-}OCH3}$	55
536.5	O 1s (O–CH_3) → σ^*_{O-CH3}	55
537.7	ZnO O 1s → 2p	56,57
540	O 1s (O–CH_3) →σ^*_{C-OCH3}	55
546	O 1s (C═O) → $\sigma^*_{C=O}$	55

beam damage. Interestingly, the intensity of this peak can also be seen to increase with the number of infiltration cycles, particularly to a relatively larger degree for AlO_x-primed-ZnO_x infiltration in comparison to AlO_x infiltration. In the oxygen K-edge spectra (Figure 5d,e), the most prominent peak at 531.5 eV corresponds to the O 1s → $\pi^*_{C=O}$ transition.[55] The intensity of this peak monotonically decreases with an increasing number of AlO_x infiltration cycles. A similar decrease in peak intensity is also seen in the case of AlO_x-primed-ZnO_x infiltration. However, it appears to have been nearly diminished by the fourth infiltration cycle with the appearance of a peak at 532.5 eV corresponding to the O 1s → 2p–Zn 3d4s transition in ZnO.[56,57] Unsurprisingly, without the AlO_x-priming, both the C 1s → $\pi^*_{C=O}$ and the O 1s → $\pi^*_{C=O}$ peaks in the respective spectra do not show any changes (Figure 5c,f), verifying that no discernible ZnO_x infiltration has taken place due to the low reactivity of DEZ with carbonyl groups in PMMA.

The normalized peak area extracted for the 1s → $\pi^*_{C=O}$ transition from both the carbon K-edge and oxygen K-edge is plotted against the number of infiltration cycles in Figure 6a,b,

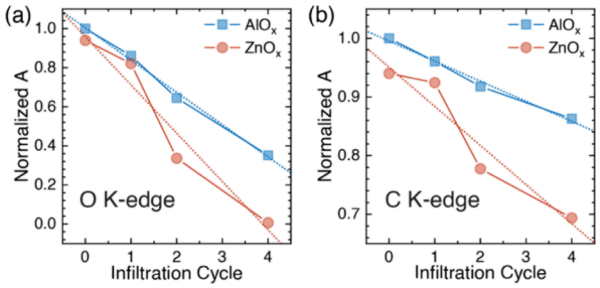

Figure 6. Evolution of the normalized peak area corresponding to the 1s C═O → π^* C═O transition with respect to the number of infiltration cycles estimated from (a) oxygen K-edge and (b) carbon K-edge NEXAFS measurements.

respectively. In both cases, the normalized area shows a steeper change for AlO_x-primed-ZnO_x infiltration compared to that for AlO_x infiltration. Note that the NEXAFS PEY spectra originate from the photoelectrons from only the topmost few nanometers of the sample. Therefore, the trends depicted in Figure 6a,b represent the chemical structure of the near-surface region. As the surface layer starts to become clogged up by AlO_x infiltration, the evolution of the normalized peak area of the 1s → $\pi^*_{C=O}$ transition lags behind that of the AlO_x-primed-ZnO_x infiltration. The trend in NEXAFS characterization draws attention to a crucial point with respect to the progression of infiltration reactions. The incremental decrease in the 1s → $\pi^*_{C=O}$ suggests that not all of the carbonyl groups get instantly consumed. In fact, they get consumed

https://doi.org/10.1021/acs.chemmater.5c02584
Chem. Mater. 2026, 38, 1751–1765

incrementally with increasing infiltration cycles, indicating incomplete yield for the carbonyl conversion reaction. Once the carbonyl groups are reacted with metal precursors, then onward they likely follow the progression laid out in Schemes 2 and 3. Therefore, several "1-cycle"-like species are created during *every* cycle, while the previously reacted sites undergo the progressive reaction depicted in Schemes 2 and 3. The hybrid material thus generated after a certain number of infiltration cycles is likely a heterogeneous mixture of all of the different types of species shown in the schematics.

While the trends in NEXAFS characterization seem to agree with QCM mass gain measurement that AlO_x-primed-ZnO_x infiltration shows higher fidelity than AlO_x, the incremental consumption of carbonyl in both of the infiltration processes raises a puzzling anomaly: As per the conventional understanding, the AlO_x-primed-ZnO_x infiltration proceeds via a hydroxyl-mediated reaction pathway, where initial hydroxyl species are generated through priming (TMA consuming carbonyl site and subsequently hydrolyzed). However, as per the NEXAFS trend, carbonyl groups in the AlO_x-primed matrix are incrementally consumed even during ZnO_x infiltration cycles, indicating that DEZ is, in fact, responsible for reacting with unreacted carbonyl groups of the AlO_x-primed matrix. On the other hand, without the AlO_x-priming, no discernible ZnO_x infiltration is observed (Figure 5c,f), indicating that DEZ by itself exhibits insufficient reactivity to carbonyl groups.

We devised a simulation procedure to obtain a deeper understanding of atomic structure evolution and the NEXAFS spectra. In principle, larger structure models are more representative of the experimental environment but also more computationally demanding. To balance computational cost and accuracy, we chose a model that can represent different infiltration scenarios and the surrounding atomic environment, small enough for efficient structure relaxation using DFT.[59] As shown in Figure S1a, the model was a short PMMA polymer chain composed of five monomers (PMMA pentamer), wherein the carbonyl groups of the three central monomer units were utilized for simulating the infiltrated molecular structure under different fractions of infiltration. The two extra terminal monomer units at each side were used to simulate the chemical environment in a PMMA polymer chain. In a long polymer chain, terminal units represent a negligible fraction of all of the carbon atoms in the whole polymer. Therefore, reactions with terminal units were not considered.

In order to estimate the relationship between the C K-edge NEXAFS spectra and the fraction of the PMMA carbonyl groups converted during infiltration, we simulated NEXAFS spectra with DFT optimized structures using multiple scattering theory for critical species throughout the infiltration process,[60,61] including pure PMMA and infiltration products with 33.3 and 66.6% of the PMMA C═O carbonyl groups "consumed" by infiltration (i.e., converted to −C−O−M−, with M denoting either Al or Zn). The spectra of each species were computed by averaging the spectra of all the individual carbon atoms of the central three monomer units (areas colored orange, green, and blue in Figure S1a) in the pentamer atomic model. The 33.3% infiltration product was simulated by attaching an $-Al(OH)_2$ or −ZnOH to the carbonyl oxygen of the central (green) monomer unit, and the 66.6% infiltration product by attaching $-Al(OH)_2$ or −ZnOH to the carbonyl oxygen of the second (orange) and the fourth (blue) monomer unit while leaving the central unit unreacted. We found that the resulting spectra were insensitive to the precursor attachment positions, particularly for the C 1s → $\pi^*_{C=O}$ peak.

Figure S1b shows the simulated NEXAFS spectra for the PMMA pentamer and its infiltrated derivatives. While the exact peak positions did not match those in the experimental spectra precisely, the simulation reproduces the key spectral features. This is mainly due to the inherent difficulty in determining a representative conformation since PMMA is a conformationally flexible molecule.[62,63] As an alternative, we developed a case-specific procedure to explore the trend of a local feature—the intensity of the peak corresponding to the transition C 1s → $\pi^*_{C=O}$. Figure S1c shows the evolution of the relative height of the C 1s → $\pi^*_{C=O}$ peak normalized to the one in the pure PMMA spectra as the infiltration produces scenarios, where 33.3 or 66.6% of the carbonyl groups are consumed during infiltration. The trend for infiltration leading to attachment of Al and Zn is highly consistent. The intensity of the peak corresponding to the C 1s → $\pi^*_{C=O}$ transition steadily decreases with the increased fraction of infiltration. To minimize the error incurred by the difference between the simulated spectra and the experimental spectra, we computed the peak intensity as a relative height (I_{rel}) for both the simulated spectra and the experimental spectra by comparing it to the peak intensity in PMMA. We performed a least-squares regression using simulated data to formulate this relationship as a linear equation: $f = 1.29 \times I_{rel} + 1.27$, with f being the fraction of the carbonyl group consumed (viz., infiltration fraction). Applying this equation to the relative peak heights extracted from the experimental spectra, we estimated the consumed carbonyl group fraction corresponding to the first, second, and fourth infiltration for both AlO_x and ZnO_x (Figure S1d). It is noted that the obtained fractions can be safely compared for monitoring relative differences. At the same time, the absolute accuracy of the values is challenging to ascertain, given the difference between the modeled PMMA pentamer vs the actual PMMA polymer chain with a much larger molecular weight. The percentage of carbonyl consumption in AlO_x infiltration was estimated to be 5.4, 13.4, and 26.7% for the first, second, and fourth infiltration cycles, respectively. The evolution of the ZnO_x infiltration fraction following AlO_x priming was faster. The Al priming led to the consumption of 18.58% of the PMMA carbonyl groups, which is a much larger amount of consumption compared to the first AlO_x infiltration cycle. This may have been caused by a shorter purging time after the TMA exposure during the priming cycle (120 vs 60 s). As demonstrated recently by Waldman et al. for group 13 oxide infiltration, a low precursor reactivity can lead to a deeper, more uniform, and greater amount of metal oxide infiltration.[19] Subsequently, the percentage of carbonyl consumption further evolved to 22.19, 42.82, and 55.51% for the first, second, and fourth ZnO_x infiltration cycles, respectively. It is evident that the fraction of carbonyl consumption increased rather rapidly for ZnO_x infiltration compared to AlO_x infiltration. The observed trends are consistent with the premise that the AlO_x-clogged topmost surface of PMMA during the AlO_x infiltration retarded the sorption of TMA molecules into the polymer matrix below, which reduced the fraction of carbonyl consumption relative to the case of ZnO_x infiltration, wherein the absence of such clogging enabled sorption of a greater number of DEZ molecules and their reaction with AlO_x-priming-activated PMMA carbonyl groups despite DEZ's lower reactivity.

https://doi.org/10.1021/acs.chemmater.5c02584
Chem. Mater. 2026, 38, 1751−1765

Mechanism of Accelerated ZnO_x Infiltration in Alumina-Priming-Activated Polymer Matrix

In order to unravel the noted anomaly observed in NEXAFS characterization and to gain a deeper insight into the molecular structural evolution during multiple infiltration cycles, we performed IRRAS, an IR spectroscopy technique that has been previously utilized for studying infiltrated inorganic species in SU-8 polymer thin films[64] and is known to provide high sensitivity in ultrathin films.[65] The evolutions of IRRAS spectra with an increasing number of infiltration cycles in three different scenarios: (a) AlO_x infiltration, (b) ZnO_x infiltration without AlO_x priming, and (c) AlO_x-primed ZnO_x infiltration are illustrated in Figure 7. Various functional groups in PMMA can be identified in IR absorption bands such as C−H stretches of the $-CH_2$ and $-CH_3$ groups at 2949 and 2997 cm^{-1}; C═O stretching at 1739 cm^{-1}, $\delta(CH_3/CH_2)$ bending at 1483 and CH_3/CH_2 scissoring/bending at 1444 cm^{-1}, symmetric CH_3 deformation ("umbrella") at 1388 cm^{-1}, and C-OR at 1153−1271 cm^{-1}. No ascertainable changes were seen in these groups except for the C═O carbonyl stretching. A slight decrease in the intensity of the carbonyl peak was found in the case of AlO_x infiltration (Figure 7a), indicating the consumption of some of the carbonyl groups. No noticeable change in carbonyl peak was found in the case of ZnO_x infiltration without AlO_x priming, which is in line with the understanding that the DEZ, on its own, lacks reactivity to carbonyl groups, and hence, negligible infiltration and hence negligible carbonyl group consumption takes place. In the case of AlO_x-primed ZnO_x infiltration, larger carbonyl peak bleaching is observed with an increasing number of ZnO_x cycles, which agrees with the NEXAFS results reported earlier in Figure 5. Interestingly, the formation of a broad new peak is observed in the IR spectra of AlO_x-primed ZnO_x infiltration at ∼1597 cm^{-1}. This IR peak at 1597 cm^{-1} is consistent with and has been previously correlated to antisymmetric OCO modes of bound carboxylate (e.g., *formate-like)* species, which are commonly observed during ALD on metal oxide surfaces.[66]

Based on these measurements, we propose a reaction mechanism likely taking place, as depicted in Scheme 4. Step A is the final byproduct of single-cycle AlO_x priming, which is the last step of the reaction, as shown in Scheme 1. When the Lewis acidic DEZ precursor is introduced in the ALD chamber, it reacts with (a) the hydroxyl group attached to the Al of the AlO_x-priming adduct and (b) the adjacent carbonyl group, which gets activated due to the partial bonding with Al of the AlO_x-priming adduct, leading to the formation of a cyclic structure by electrostatic interactions as shown in Step B. Further rearrangements of the adduct species lead to the *dealkylation* of the adjacent ester (methacrylate) group and formation of a stable, cyclic resonant structure, resulting in a *formate* functional group connected to Zn, as depicted in Step C. As compared to the total number of C−O−R (ester) groups present in the PMMA film, only a small fraction participates in the infiltration reactions and thus undergoes dealkylation. Therefore, C−O−R absorption does not significantly change in Figure 7c. However, the appearance of a new peak at 1597 cm^{-1} strongly implied the generation of formate species, which can only be formed by dealkylation. A similar dealkylation reaction has been reported by the Losego group recently during VPI of $TiCl_4$ into PMMA.[67] Finally, during the water half-cycle, this adduct is hydrolyzed and forms the final product of ZnO_x infiltration, as illustrated in step D.

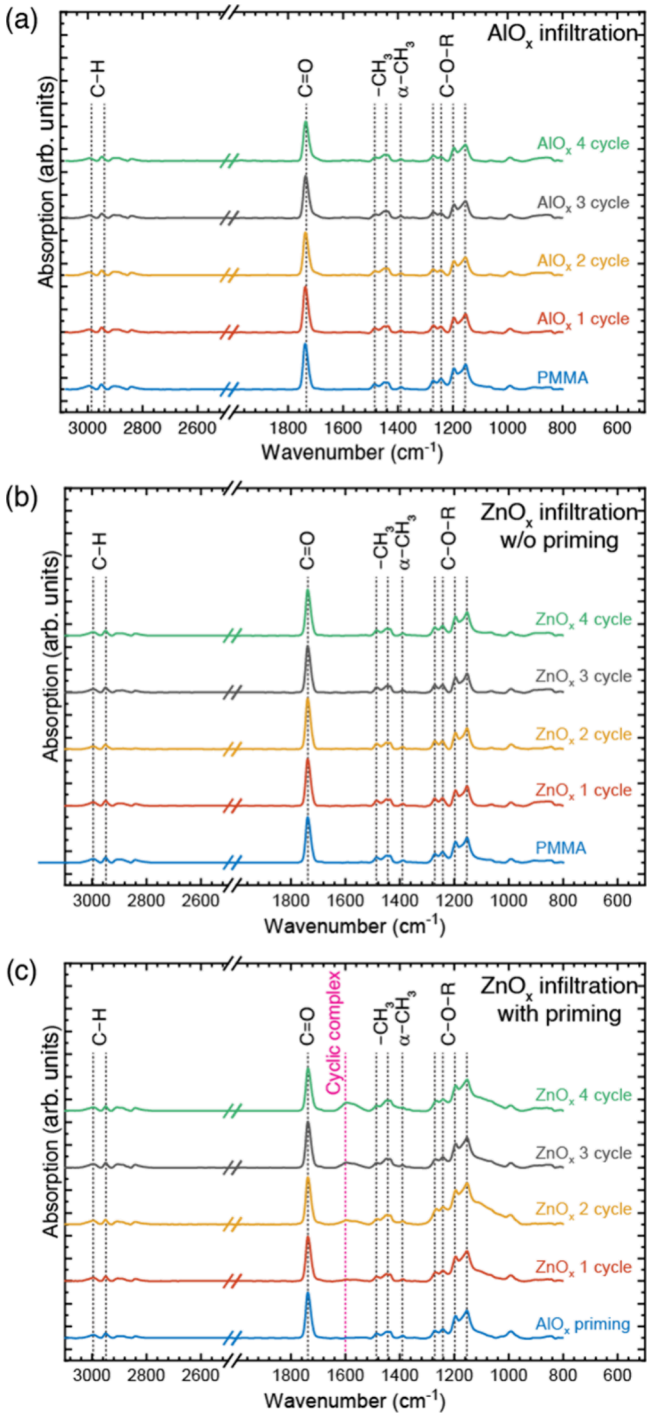

Figure 7. (a) Evolution of IRRAS spectra with an increasing number of AlO_x infiltration cycles, exhibiting a slight bleaching of the carbonyl peak. (b) IRRAS spectra with different numbers of ZnO_x infiltration cycles without applying AlO_x priming, depicting negligible change in the carbonyl peak. (c) IRRAS spectra from AlO_x-primed ZnO_x infiltration evolving with an increasing number of ZnO_x cycles. Not only does the carbonyl peak exhibit bleaching with respect to C−O−R peaks as the ZnO_x infiltration cycles increase but also a new peak (indicated with a magenta line) is formed and strengthened at ≈1597 cm^{-1}, which is hypothesized to be related to the formation of the Zn cyclic adduct.

To understand the consequence of AlO_x priming for DEZ-infiltration reactions and to ascertain probability of formation of various species in the infiltration flow, we simulated the

https://doi.org/10.1021/acs.chemmater.5c02584
Chem. Mater. 2026, 38, 1751−1765

Scheme 4. Proposed Mechanism of AlO_x-Primed ZnO_x Infiltration via Cyclic Adduct Formation[a]

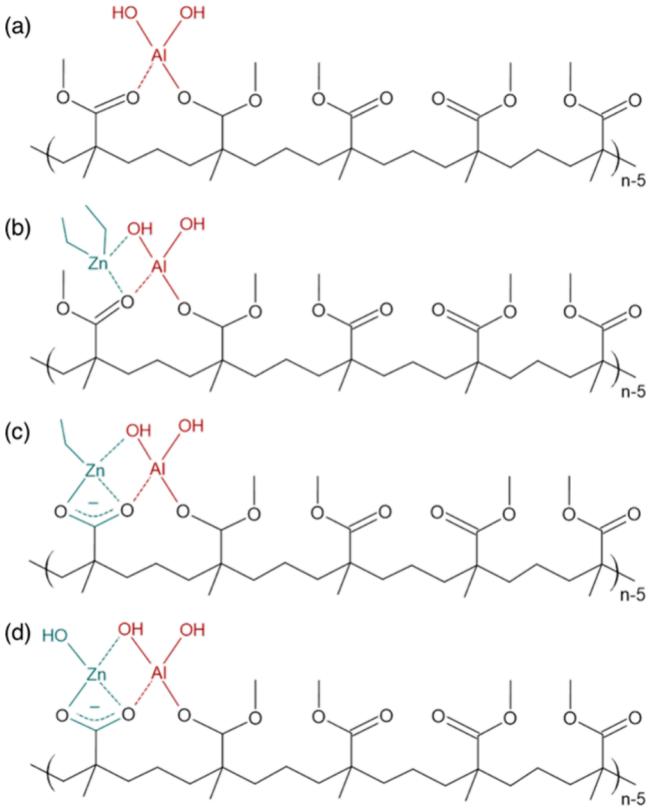

[a](a) Chemical structure of 1-cycle alumina-primed PMMA matrix (final stage of reaction Scheme 1); (b) Al-containing cyclic adduct activates the adjacent carbonyl group, making it a susceptible site for DEZ to react to (c) formation of a stable, cyclic resonant structure between two adjacent *formate* species and Zn (d) when subjected to water in the second half-cycle of infiltration, hydrolysis leads to the formation of −Zn(OH) species at the metal infiltration site.

formation energy of the DEZ-carbonyl group Lewis adduct using DFT[59,68] at two different schemes: (1) *sp2* (carbonyl) carbon in pristine PMMA pentamer and (2) *sp2* (carbonyl) carbon where the adjacent carbonyl group has undergone AlO_x priming (step A in Scheme 4). It turns out that the reaction with the pristine PMMA pentamer is exothermic with a formation energy of −151.9 kJ/mol. However, it becomes even more exothermic when preceded by the AlO_x priming process (conversion reaction from step A to step B in Scheme 4) with a formation energy of −185.4 kJ/mol. In both cases, the reaction leads to carbonyl group consumption and results in C 1s → $\pi^*_{C=O}$ and O 1s → $\pi^*_{C=O}$ peak intensity changes in carbon and oxygen K-edge NEXAFS spectra in Figure 5b,d, respectively. The atomic charges induced by the AlO_x priming adduct can potentially play a role. Still, it will not be strong enough to cause any significant difference since it is 4 bonds away from the adjacent carbonyl group. It turns out that enhanced reactivity is a result of direct interaction between DEZ and the hydrated AlO_x adduct group. The relaxed structure of the Lewis adduct in Figure 8a (steps B and C) shows that extra coordination bonds have formed between the Zn atom from DEZ and the oxygen atom from the hydrated AlO_x adduct. The network of additional bonds enriched by AlO_x priming stabilizes the Zn Lewis adduct. This stabilization effect is further enhanced after the *dealkylation* reaction and becomes energetically favorable (conversion from step B to step C with a formation energy of −112.5 kJ/mol). Finally, the conversion from step C to step D in Scheme 4 takes place during the hydrolysis half-cycle with a formation energy of −55.2 kJ/mol, and the relaxed structure at step D is shown in Figure 8a (step D). It is perceived that the formed adduct structure is responsible for the manifestation of a new peak at the wavenumber 1600 cm^{-1}. We also simulated IR absorption spectra for Scheme 4 steps A−D, which are depicted in Figure 8b. It can be seen that a new peak, corresponding to the *formate* C−O bond stretches, appears in simulated IR spectra for step C at 1588.5 cm^{-1}, in agreement with experimental results. After hydrolysis, this additional peak persists in simulated spectra for step D, while it undergoes a 12.4 cm^{-1} redshift.

Local Structures of Infiltrated ZnO_x from Zn-Edge NEXAFS

We further investigated the local structure of the infiltrated ZnO_x using NEXAFS measurements carried out at the Zn L-edge (PEY spectra shown in Figure 9a). Zn L3-edge peaks are assigned based on prior reports, as illustrated in Table 3. Most prominently, the 4-cycle ZnO_x-infiltrated sample showed a peak at ∼1022 eV that corresponds to the 2p → Zn 4p electron transition.[69] This peak was significantly less prominent for the samples with fewer infiltration cycles. The spectrum for a one-cycle ZnO_x-infiltrated sample showed a pre-edge shoulder peak at ∼1018 eV, which corresponds to structural disorder or defects.[69] It has also been inferred that it suggests asymmetry in the wurtzite structure.[70] As the number of infiltration cycles is increased, the presence of the shoulder peak becomes weaker. The peak at ∼1027 eV, distinguishable only in the 4-cycle infiltrated sample, represents a weaker d-d interaction of the neighboring Zn atoms.[69,70] In order to gauge the relative contributions of the peaks, we used multiple Gaussian fits for various prominent features of the spectra, which are illustrated in Figure S2a−c.

We find that the peak at ≈1018 eV, which is initially sharper for one-cycle infiltration, becomes increasingly broader with more infiltration cycles. In contrast, the peak at ≈1022 eV becomes increasingly sharper with the increasing number of infiltration cycles. The fitted area of the Gaussians is plotted against the number of infiltration cycles in Figure 9b, along with the ratio of the fitted area of the 1022 eV peak to that of the 1018 eV peak. Clearly, the p → d/p peak area shows only a marginal increase compared to the significant growth for the Zn 2p → 4p peak area, suggesting that with increasing infiltration of ZnO_x, the relative disorder or asymmetry reduces. In fact, the granular morphology of ZnO_x can be seen in the cross-section HAADF image of the 4-cycle ZnO_x-infiltrated PMMA film (Figure 4b).

CONCLUSIONS

In conclusion, we have performed a comparative study on the VPI of AlO_x and AlO_x-primed ZnO_x into PMMA to understand the evolution of the local molecular structure. Based on the analyses of the QCM mass gain, cross-sectional STEM structural characterization, and NEXAFS spectroscopy data, further rationalized by DFT and FEFF-based simulations, we found that for AlO_x infiltration in PMMA, the hyper-branching of AlO_x molecular network can cause rapid clogging of the PMMA free volume near the top surface, leading to the AlO_x infiltration saturating quickly, while for ZnO_x infiltration, it can lead to accelerated, more sustained, and deeper ZnO_x

https://doi.org/10.1021/acs.chemmater.5c02584
Chem. Mater. 2026, 38, 1751−1765

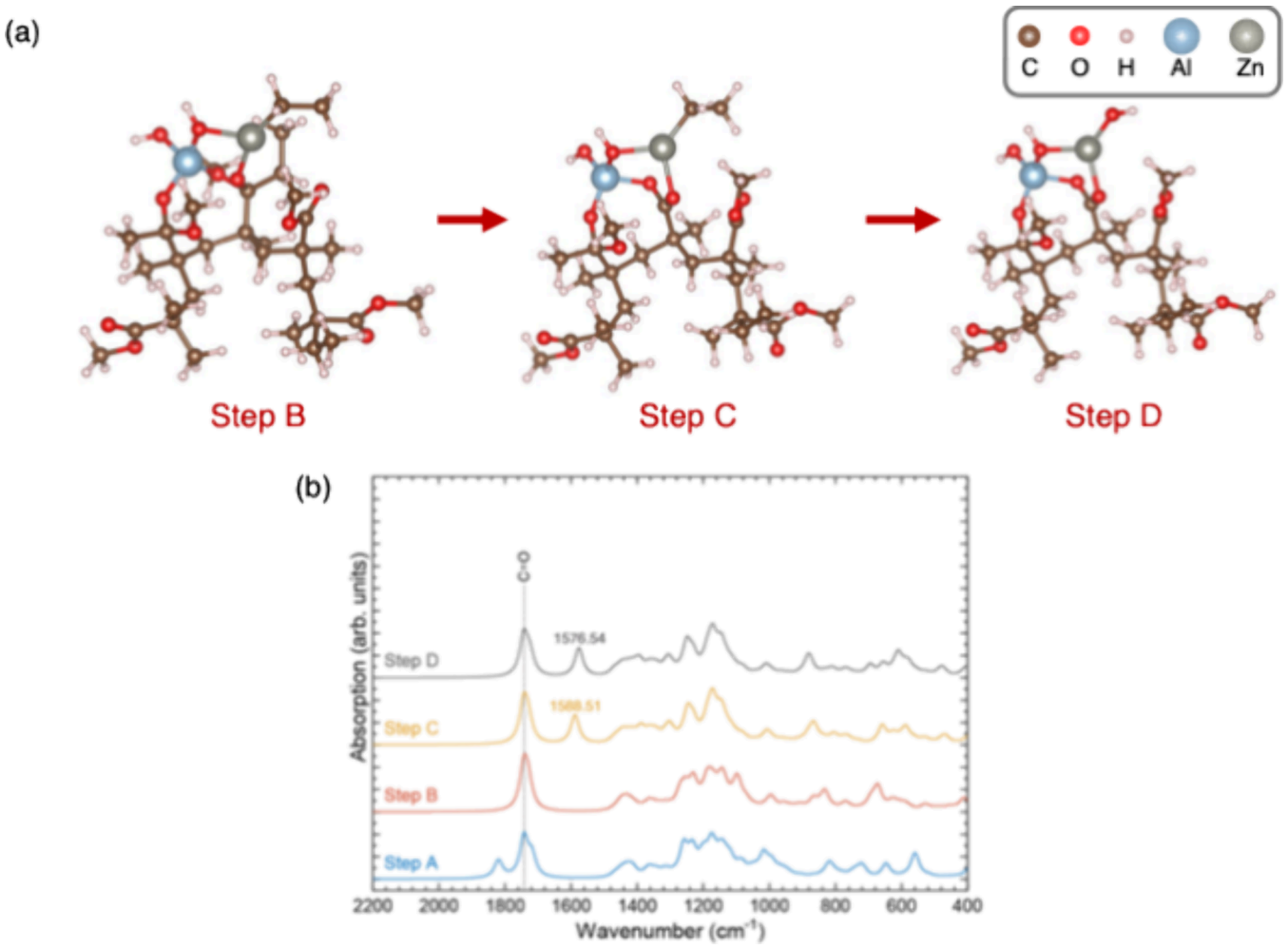

Figure 8. (a) Schematic illustration of AlO_x-primed ZnO_x infiltration process via cyclic adduct formation with adjacent *sp2* (carbonyl) carbon during the first half-cycle of DEZ exposure (Step B), converting the carbon to *sp3* and turning partially sp2 after the *dealkylation* reaction in the form of a negatively charged, resonant format group (step C). The cyclic adduct survives even after hydrolysis at the end of the first full cycle (step D). (b) Simulated IR spectra for steps A−D. A new peak, corresponding to the *formate* C−O bond stretches, can be seen to have appeared in step C, which undergoes redshift in step D.

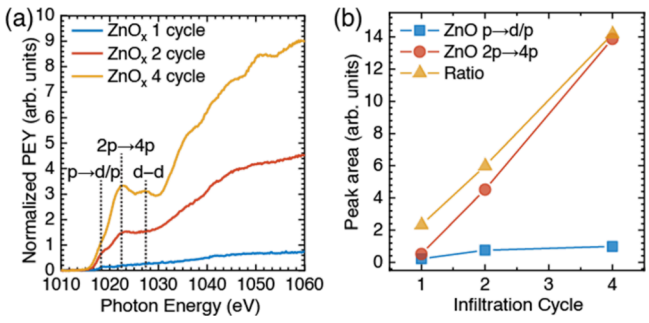

Figure 9. (a) NEXAFS spectra acquired at Zn L-edge for AlO_x-primed ZnO_x-infiltrated samples with different numbers of Zn cycles, depicting ZnO peaks corresponding to 2p → 4p transition getting increasingly prominent with increasing numbers of infiltration cycles. (b) Evolution of the Gaussian peak area of p → d/p and 2p → 4p along with their ratio.

infiltration in PMMA as a consequence of the heightened reactivity of polymer matrix itself (i.e., carbonyl group) toward DEZ activated by the AlO_x priming step. Though precursor reactivity, in general, plays a significant role in determining the overall infiltration depth and fidelity, the results reveal that the evolution of infiltration over multiple cycles can also be influenced by the infiltration history, the ease of precursor sorption into the matrix, and, importantly, the enhanced reactivity of organic functional groups itself activated by the preinfiltrated species. These factors need to be considered holistically for designing and engineering high-fidelity inorganic VPI procedures in polymers for functional organic−inorganic hybrid material synthesis.

Table 3. Peak Assignment for Zn L3-Edge

energy (eV)	assignment	refs
1018	p → d/p (asymmetric wurtzite)	69,70
1021.8	Zn 2p → 4p	69,70
1026.7	Weak d − d interaction of Zn 4d	69,70

EXPERIMENTAL METHODOLOGIES

Sample Preparation

A commercial stock solution of PMMA 950 A2 (2 wt % in anisole, a molecular weight of 950,000 g mol^{-1}, MicroChem) was further diluted using Anisole (Sigma-Aldrich) to a 1 wt % solution, which was then spin-coated on cleaned Si substrates at 83 Hz (5000 rpm) for 60 s. Spun substrates were then applied post-application bake of 3 min at

https://doi.org/10.1021/acs.chemmater.5c02584
Chem. Mater. 2026, 38, 1751−1765

180 °C. The thin film thickness was estimated to be ∼25 nm using a J.A. Woollam spectroscopic ellipsometer. For the QCM mass gain measurement experiment, AT-cut quartz crystals operating at 6 MHz with a gold surface were spin-coated with PMMA thin films with the same processing conditions used for Si substrates.

Vapor-Phase Infiltration

The Cambridge Nanotech Savannah S100 commercial ALD system was used for VPI at 85 °C. The exposure steps for all precursors (TMA, DEZ, and water) described next were preceded by 30 s chamber evacuation and performed under a static vacuum (i.e., isolating the chamber from the pump by closing the gate valve). The purging steps with 10^{-4} m^3/min (100 sccm) N2 flow were carried out under a dynamic vacuum (i.e., the chamber was actively evacuated by opening the gate valve).

During AlO_x infiltration, each infiltration cycle consisted of TMA exposure (half-cycle) for a 30 s period during which the TMA was pulsed for 14 ms 3 times at 10 s intervals (microdose protocol), followed by 2 min of chamber purge and 30 s of chamber evacuation. Subsequently, the oxidation half-cycle consisted of 30 s exposure to water vapor during which water was pulsed for 40 ms 3 times at 10 s intervals (microdose protocol), followed by another 2 min chamber purge and 30 s chamber evacuation.

For AlO_x-primed ZnO_x infiltration, the single AlO_x priming cycle consisted of 30 s of static TMA exposure initiated by a single 14 ms TMA pulse, followed by a 1 min N_2 purge step and a 30 s chamber evacuation. Subsequently, 60 s static water vapor exposure was initiated by a single 40 ms water pulse, followed by a 2 min N_2 purge step and a 30 s chamber evacuation. Afterward, without breaking the vacuum, samples were subjected to four ZnO_x microdose infiltration cycles using DEZ and water precursors. During the first half-cycle, DEZ exposure was carried out for 60 s, during which DEZ was pulsed for 200 ms 6 times at 10 s intervals, followed by a 2 min chamber purge and a 30 s chamber evacuation. Subsequently, the water vapor half-cycle was implemented for 60 s, during which water was pulsed for 40 ms 6 times at 10 s intervals, followed by purging the unreacted water vapor using N_2 flow for 2 min and 30 s chamber evacuation.

NEXAFS Measurements

Spectroscopic characterization using the NEXAFS technique was carried out at the 7-ID-1 beamline at the National Synchrotron Light Source II at the Brookhaven National Laboratory.[71,72] Samples were mounted with conductive tape to the measurement bar. Both total and partial electron yields (TEY and PEY, respectively) as well as fluorescence modes were collected. During the PEY measurements, the grid bias used for the carbon k-edge was −50 V, for the oxygen k-edge was −300 V, and for the Zn L-edge was −500 V. Analysis was conducted using the QANT package using double normalization via the stable reference method using a gold mesh upstream and a photodiode. Multipeak fitting was performed within QANT, identifying a minimal set of peaks and fixing the respective energy and width of each peak across samples, fitting the peak height of each peak for each sample for comparison.[73]

Transmission Electron Microscopy

The samples for cross-sectional TEM analysis were prepared using a standard in situ lift-out procedure using Ga ion milling in an FEI Helios 600 Nanolab focused ion beam system. An FEI Talos F200X 200 kV STEM system equipped with an EDS elemental mapping capability was used for acquiring STEM images.

Computational Simulation

A short PMMA chain consisting of 5 monomer units (Figure S1a) was modeled atomically to simulate the structure of PMMA and the infiltration reactions. The ωB97M-V functional[74] is used for geometry optimization, vibrational frequency analysis, single point energy evaluations, which has been reported to accurately describe both covalent and noncovalent interactions. All of the structures have been confirmed to be true minima by having no imaginary frequencies. For geometry optimization and vibrational frequency analysis, the 6-31G(d,p) basis set is applied to C, H, and Al atoms, the def2-SVP basis set is applied to Zn atoms, while the diffuse function enhanced 6-31+G(d,p) basis set is applied to O atoms. For single point energy evaluation, larger basis sets, 6-311++G(d,p) and def2-TZVPD, are used for C, H, and Zn, respectively. The vibrational frequencies is multiplied by a scaling factor 0.959[75] for infrared spectrum predictions. The multiple scattering theory simulations of K-edge (C 1s) NEXAFS spectra are conducted using the FEFF program package.[60,61]

We note that we employ a deliberately simplified modeling approach in this work aimed at capturing the primary driving forces governing infiltration as well as the key spectroscopic features. This model inevitably neglects cage effects associated with confinement, entropy effects arising from molecular configurations and thermal motion, and long-range synergistic interactions with the surrounding polymer environment. Consequently, this simplification involves a trade-off in quantitative accuracy, and the computational results are therefore aimed to be interpreted qualitatively rather than quantitatively.

IRRAS Measurements

A Bruker Vertex 80 spectrometer equipped with an HgCdTe detector was used to acquire the IRRAS spectra. The grazing incidence angle of 8° under ultrahigh vacuum conditions (10^{-8} mbar) for measurements. The spectral data were collected with a resolution of 2 cm^{-1} over the wavenumber range of 800−4000 cm^{-1}.

■ ASSOCIATED CONTENT

Supporting Information

The Supporting Information is available free of charge at https://pubs.acs.org/doi/10.1021/acs.chemmater.5c02584.

Representation of PMMA pentamer model used for simulations, simulated NEXAFS spectra, peak evolution and estimated infiltration fraction, simultaneous multiple Gaussian fit for Zn-edge spectra (PDF)

■ AUTHOR INFORMATION

Corresponding Authors

Nikhil Tiwale − *Center for Functional Nanomaterials, Brookhaven National Laboratory, Upton, New York 11973, United States;* orcid.org/0000-0001-8229-7108; Email: ntiwale@bnl.gov

Xiaohui Qu − *Center for Functional Nanomaterials, Brookhaven National Laboratory, Upton, New York 11973, United States;* Email: xiaqu@bnl.gov

Chang-Yong Nam − *Center for Functional Nanomaterials, Brookhaven National Laboratory, Upton, New York 11973, United States; Department of Materials Science and Chemical Engineering, Stony Brook University, Stony Brook, New York 11794, United States;* orcid.org/0000-0002-9093-4063; Email: cynam@bnl.gov

Authors

Ashwanth Subramanian − *Department of Materials Science and Chemical Engineering, Stony Brook University, Stony Brook, New York 11794, United States*

Sayantani Sikder − *Department of Materials Science and Chemical Engineering, Stony Brook University, Stony Brook, New York 11794, United States*

Guillaume Freychet − *National Synchrotron Light Source II, Brookhaven National Laboratory, Upton, New York 11973, United States; University of Grenoble Alpes, CEA, Leti, Grenoble F-38000, France*

Eliot Gann − *National Synchrotron Light Source II, Brookhaven National Laboratory, Upton, New York 11973,*

United States; Material Measurement Laboratory, National Institute of Standards and Technology, Gaithersburg, Maryland 20899, United States

Cherno Jaye − *Material Measurement Laboratory, National Institute of Standards and Technology, Gaithersburg, Maryland 20899, United States*

Kim Kisslinger − *Center for Functional Nanomaterials, Brookhaven National Laboratory, Upton, New York 11973, United States*

Jorge Anibal Boscoboinik − *Center for Functional Nanomaterials, Brookhaven National Laboratory, Upton, New York 11973, United States; Department of Materials Science and Chemical Engineering, Stony Brook University, Stony Brook, New York 11794, United States;* orcid.org/0000-0002-5090-7079

Complete contact information is available at: https://pubs.acs.org/10.1021/acs.chemmater.5c02584

Author Contributions

N.T., A.S., and C.-Y.N. perceived the concept. C.-Y.N. supervised the project. N.T. and A.S. performed sample preparation and infiltration synthesis. C.J., G.F., and E.G. performed NEXAFS characterization and interpreted the spectra. X.Q. performed and interpreted computational simulations. K.K. performed TEM characterization. S.S. and J.A.B. performed IRRAS measurements and analyzed the spectra. N.T. and C.-Y.N. cowrote the manuscript. All authors reviewed and finalized the manuscript.

Notes

The authors declare no competing financial interest.

■ ACKNOWLEDGMENTS

This research is supported by the U.S. Department of Energy Office of Science Accelerate Initiative Award 2023-BNL-NC033-Fund. This research used the Materials Synthesis & Characterization, Nanofabrication, Electron Microscopy, Proximal Probes, and Theory & Computation Facilities at the Center for Functional Nanomaterials (CFN) and the Spectroscopy Soft and Tender (SST-1) beamline (7-ID-1) of the National Synchrotron Light Source II (NSLS-II), which are U.S. Department of Energy Office of Science User Facilities, at Brookhaven National Laboratory (BNL) under contract no. DE-SC0012704. Certain commercial equipment, instruments, materials, suppliers, or software are identified in this paper to foster understanding. Such identification does not imply recommendation or endorsement by the National Institute of Standards and Technology (NIST), nor does it imply that the materials or equipment identified are necessarily the best available for the purpose.

■ REFERENCES

(1) Subramanian, A.; Tiwale, N.; Nam, C.-Y. Review of Recent Advances in Applications of Vapor-Phase Material Infiltration Based on Atomic Layer Deposition. *JOM* **2019**, *71* (1), 185−196.

(2) Ingram, W. F.; Jur, J. S. Properties and Applications of Vapor Infiltration into Polymeric Substrates. *JOM* **2019**, *71* (1), 238−245.

(3) Berman, D.; Shevchenko, E. Design of Functional Composite and All-Inorganic Nanostructured Materials via Infiltration of Polymer Templates with Inorganic Precursors. *J. Mater. Chem. C* **2020**, *8* (31), 10604−10627.

(4) Waldman, R. Z.; Mandia, D. J.; Yanguas-Gil, A.; Martinson, A. B. F.; Elam, J. W.; Darling, S. B. The Chemical Physics of Sequential Infiltration Synthesis—A Thermodynamic and Kinetic Perspective. *J. Chem. Phys.* **2019**, *151* (19), 190901.

(5) Nam, C.-Y.; Stein, A.; Lu, M.; Kim, J.; Tiwale, N.; Hwang, S. M.; Subramanian, A.; *Inorganic-Infiltrated Polymer Hybrid Thin Film Resists for Advanced Lithography*. US Patent App. 16/808661, 2020.

(6) Tiwale, N.; Subramanian, A.; Kisslinger, K.; Lu, M.; Kim, J.; Stein, A.; Nam, C.-Y. Advancing next Generation Nanolithography with Infiltration Synthesis of Hybrid Nanocomposite Resists. *J. Mater. Chem. C* **2019**, *7* (29), 8803−8812.

(7) Tiwale, N.; Subramanian, A.; Kisslinger, K.; Lu, M.; Kim, J.; Stein, A.; Nam, C.-Y. *Infiltration Synthesis of Hybrid Nanocomposite Resists for Advanced Nanolithography*. In Proceedings of SPIE 11326, Advances in Patterning Materials and Processes XXXVII; Gronheid, R., Sanders, D. P., Eds.; SPIE, 2020; p 113260J. .

(8) Tiwale, N.; Subramanian, A.; Freychet, G.; Gann, E.; Kisslinger, K.; Lu, M.; Stein, A.; Kim, J.; Nam, C.-Y. *Hybrid Resist Synthesis by Ex-Situ Vapor-Phase Infiltration of Metal Oxides into Conventional Organic Resists*. In Proceedings of SPIE 11612, Advances in Patterning Materials and Processes XXXVIII; SPIE, 2021; p 116120A. .

(9) Subramanian, A.; Tiwale, N.; Lee, W.; Kisslinger, K.; Lu, M.; Stein, A.; Kim, J.; Nam, C. Vapor-Phase Infiltrated Organic−Inorganic Positive-Tone Hybrid Photoresist for Extreme UV Lithography. *Adv. Mater. Interfaces* **2023**, *10* (28), 2300420.

(10) Tseng, Y.-C.; Peng, Q.; Ocola, L. E.; Czaplewski, D. A.; Elam, J. W.; Darling, S. B. Enhanced Polymeric Lithography Resists via Sequential Infiltration Synthesis. *J. Mater. Chem.* **2011**, *21* (32), 11722.

(11) Checco, A.; Rahman, A.; Black, C. T. Robust Superhydrophobicity in Large-Area Nanostructured Surfaces Defined by Block-Copolymer Self Assembly. *Adv. Mater.* **2014**, *26* (6), 886−891.

(12) Marneffe, J.-F. de; Chan, B. T.; Spieser, M.; Vereecke, G.; Naumov, S.; Vanhaeren, D.; Wolf, H.; Knoll, A. W. Conversion of a Patterned Organic Resist into a High Performance Inorganic Hard Mask for High Resolution Pattern Transfer. *ACS Nano* **2018**, *12* (11), 11152−11160.

(13) Obuchovsky, S.; Frankenstein, H.; Vinokur, J.; Hailey, A. K.; Loo, Y.-L.; Frey, G. L. Mechanism of Metal Oxide Deposition from Atomic Layer Deposition inside Nonreactive Polymer Matrices: Effects of Polymer Crystallinity and Temperature. *Chem. Mater.* **2016**, *28* (8), 2668−2676.

(14) Gregory, S. A.; Li, Y.; Monroe, T. D.; Li, J.; Yee, S. K.; Losego, M. D. Vapor Phase Infiltration Doping of the Semiconducting Polymer Poly(Aniline) with TiCl 4 + H 2 O: Mechanisms, Reaction Kinetics, and Electrical and Optical Properties. *ACS Appl. Polym. Mater.* **2021**, *3* (2), 720−729.

(15) Wang, W.; Chen, C.; Tollan, C.; Yang, F.; Beltrán, M.; Qin, Y.; Knez, M. Conductive Polymer−Inorganic Hybrid Materials through Synergistic Mutual Doping of the Constituents. *ACS Appl. Mater. Interfaces* **2017**, *9* (33), 27964−27971.

(16) Nam, C.-Y.; Stein, A.; Kisslinger, K.; Black, C. T. Electrical and Structural Properties of ZnO Synthesized via Infiltration of Lithographically Defined Polymer Templates. *Appl. Phys. Lett.* **2015**, *107* (20), 203106.

(17) Nam, C.-Y.; Stein, A. Extreme Carrier Depletion and Superlinear Photoconductivity in Ultrathin Parallel-Aligned ZnO Nanowire Array Photodetectors Fabricated by Infiltration Synthesis. *Adv. Opt. Mater.* **2017**, *5* (24), 1700807.

(18) Subramanian, A.; Doerk, G.; Kisslinger, K.; Yi, D. H.; Grubbs, R. B.; Nam, C.-Y. Three-Dimensional Electroactive ZnO Nanomesh Directly Derived from Hierarchically Self-Assembled Block Copolymer Thin Films. *Nanoscale* **2019**, *11* (19), 9533−9546.

(19) Waldman, R. Z.; Jeon, N.; Mandia, D. J.; Heinonen, O.; Darling, S. B.; Martinson, A. B. F. Sequential Infiltration Synthesis of Electronic Materials: Group 13 Oxides via Metal Alkyl Precursors. *Chem. Mater.* **2019**, *31* (14), 5274−5285.

(20) Taggart, A. D.; Jeon, N.; Rozyyev, V.; Karapetrova, E.; Zaluzec, N. J.; Waldman, R. Z.; Darling, S. B.; Elam, J. W.; Martinson, A. B. F. Electronic Conductivity of Nanoporous Indium Oxide Derived from

Sequential Infiltration Synthesis. *J. Phys. Chem. C* **2021**, *125* (38), 21191−21198.
(21) Akyildiz, H. I.; Stano, K. L.; Roberts, A. T.; Everitt, H. O.; Jur, J. S. Photoluminescence Mechanism and Photocatalytic Activity of Organic−Inorganic Hybrid Materials Formed by Sequential Vapor Infiltration. *Langmuir* **2016**, *32* (17), 4289−4296.
(22) Akyildiz, H. I.; Mousa, M. B. M.; Jur, J. S. Atmospheric Pressure Synthesis of Photoluminescent Hybrid Materials by Sequential Organometallic Vapor Infiltration into Polyethylene Terephthalate Fibers. *J. Appl. Phys.* **2015**, *117* (4), No. 045301.
(23) Ocola, L. E.; Wang, Y.; Divan, R.; Chen, J. Multifunctional UV and Gas Sensors Based on Vertically Nanostructured Zinc Oxide: Volume Versus Surface Effect. *Sensors* **2019**, *19* (9), 2061.
(24) Barry, E.; Mane, A. U.; Libera, J. A.; Elam, J. W.; Darling, S. B. Advanced Oil Sorbents Using Sequential Infiltration Synthesis. *J. Mater. Chem. A* **2017**, *5* (6), 2929−2935.
(25) Zhou, C.; Segal-Peretz, T.; Oruc, M. E.; Suh, H. S.; Wu, G.; Nealey, P. F. Fabrication of Nanoporous Alumina Ultrafiltration Membrane with Tunable Pore Size Using Block Copolymer Templates. *Adv. Funct. Mater.* **2017**, *27* (34), 1701756.
(26) McGuinness, E. K.; Zhang, F.; Ma, Y.; Lively, R. P.; Losego, M. D. Vapor Phase Infiltration of Metal Oxides into Nanoporous Polymers for Organic Solvent Separation Membranes. *Chem. Mater.* **2019**, *31* (15), 5509−5518.
(27) Hu, L.; Lee, W.-I.; Subramanian, A.; Deng, E.; Kisslinger, K.; Fan, S.; Bui, V. T.; Ding, Y.; Nam, C.-Y.; Lin, H. Few-Cycle Atomic Layer Deposition to Nanoengineer Polybenzimidazole for H2/CO2 Separation. *Chem. Eng. J.* **2024**, *479*, No. 147401.
(28) Gong, B.; Spagnola, J. C.; Parsons, G. N. Hydrophilic Mechanical Buffer Layers and Stable Hydrophilic Finishes on Polydimethylsiloxane Using Combined Sequential Vapor Infiltration and Atomic/Molecular Layer Deposition. *J. Vac. Sci. Technol. A Vacuum, Surfaces, Film.* **2012**, *30* (1), No. 01A156.
(29) Azpitarte, I.; Zuzuarregui, A.; Ablat, H.; Ruiz-Rubio, L.; López-Ortega, A.; Elliott, S. D.; Knez, M. Suppressing the Thermal and Ultraviolet Sensitivity of Kevlar by Infiltration and Hybridization with ZnO. *Chem. Mater.* **2017**, *29* (23), 10068−10074.
(30) Dusoe, K. J.; Ye, X.; Kisslinger, K.; Stein, A.; Lee, S.-W.; Nam, C.-Y. Ultrahigh Elastic Strain Energy Storage in Metal-Oxide-Infiltrated Patterned Hybrid Polymer Nanocomposites. *Nano Lett.* **2017**, *17* (12), 7416−7423.
(31) Li, Z.; He, J.; Subramanian, A.; Tiwale, N.; Dusoe, K. J.; Nam, C.-Y.; Li, Y.; Lee, S.-W. Unraveling the Ultrahigh Modulus of Resilience of Core-Shell SU-8 Nanocomposite Nanopillars Fabricated by Vapor-Phase Infiltration. *Mater. Des.* **2023**, *227*, No. 111770.
(32) Akyildiz, H. I.; Padbury, R. P.; Parsons, G. N.; Jur, J. S. Temperature and Exposure Dependence of Hybrid Organic−Inorganic Layer Formation by Sequential Vapor Infiltration into Polymer Fibers. *Langmuir* **2012**, *28* (44), 15697−15704.
(33) Weisbord, I.; Shomrat, N.; Azoulay, R.; Kaushansky, A.; Segal-Peretz, T. Understanding and Controlling Polymer−Organometallic Precursor Interactions in Sequential Infiltration Synthesis. *Chem. Mater.* **2020**, *32* (11), 4499−4508.
(34) Cianci, E.; Nazzari, D.; Seguini, G.; Perego, M. Trimethylaluminum Diffusion in PMMA Thin Films during Sequential Infiltration Synthesis: In Situ Dynamic Spectroscopic Ellipsometric Investigation. *Adv. Mater. Interfaces* **2018**, *5* (20), 1801016.
(35) Caligiore, F. E.; Nazzari, D.; Cianci, E.; Sparnacci, K.; Laus, M.; Perego, M.; Seguini, G. Effect of the Density of Reactive Sites in P(S-r -MMA) Film during Al 2 O 3 Growth by Sequential Infiltration Synthesis. *Adv. Mater. Interfaces* **2019**, *6* (12), 1900503.
(36) Lee, S.; Subramanian, A.; Tiwale, N.; Kisslinger, K.; Mumtaz, M.; Shi, L.-Y.; Aissou, K.; Nam, C.-Y.; Ross, C. A. Resolving Triblock Terpolymer Morphologies by Vapor-Phase Infiltration. *Chem. Mater.* **2020**, *32* (12), 5309−5316.
(37) Biswas, M.; Libera, J. A.; Darling, S. B.; Elam, J. W. New Insight into the Mechanism of Sequential Infiltration Synthesis from Infrared Spectroscopy. *Chem. Mater.* **2014**, *26* (21), 6135−6141.
(38) Dandley, E. C.; Needham, C. D.; Williams, P. S.; Brozena, A. H.; Oldham, C. J.; Parsons, G. N. Temperature-Dependent Reaction between Trimethylaluminum and Poly(Methyl Methacrylate) during Sequential Vapor Infiltration: Experimental and Ab Initio Analysis. *J. Mater. Chem. C* **2014**, *2* (44), 9416−9424.
(39) Peng, Q.; Tseng, Y. C.; Darling, S. B.; Elam, J. W. A Route to Nanoscopic Materials via Sequential Infiltration Synthesis on Block Copolymer Templates. *ACS Nano* **2011**, *5* (6), 4600−4606.
(40) Kim, J. J.; Suh, H. S.; Zhou, C.; Mane, A. U.; Lee, B.; Kim, S.; Emery, J. D.; Elam, J. W.; Nealey, P. F.; Fenter, P.; Fister, T. T. Mechanistic Understanding of Tungsten Oxide In-Plane Nanostructure Growth via Sequential Infiltration Synthesis. *Nanoscale* **2018**, *10* (7), 3469−3479.
(41) Ocola, L. E.; Connolly, A.; Gosztola, D. J.; Schaller, R. D.; Yanguas-Gil, A. Infiltrated Zinc Oxide in Poly(Methyl Methacrylate): An Atomic Cycle Growth Study. *J. Phys. Chem. C* **2017**, *121* (3), 1893−1903.
(42) Azoulay, R.; Shomrat, N.; Weisbord, I.; Atiya, G.; Segal-Peretz, T. Metal Oxide Heterostructure Array via Spatially Controlled−Growth within Block Copolymer Templates. *Small* **2019**, *15* (51), 1904657.
(43) Tiwale, N.; Senanayak, S. P.; Rubio-Lara, J.; Alaverdyan, Y.; Welland, M. E. Optimization of Transistor Characteristics and Charge Transport in Solution Processed ZnO Thin Films Grown from Zinc Neodecanoate. *Electron. Mater. Lett.* **2019**, *15* (6), 702−711.
(44) Tiwale, N.; Senanayak, S. P.; Rubio-Lara, J.; Prasad, A.; Aziz, A.; Alaverdyan, Y.; Welland, M. E. Solution-Processed High-Performance ZnO Nano-FETs Fabricated with Direct-Write Electron-Beam-Lithography-Based Top-Down Route. *Adv. Electron. Mater.* **2021**, *7* (3), 2000978.
(45) Tiwale, N. Zinc Oxide Nanowire Gas Sensors: Fabrication, Functionalisation and Devices. *Mater. Sci. Technol.* **2015**, *31* (14), 1681−1697.
(46) Aziz, A.; Tiwale, N.; Hodge, S. A.; Attwood, S. J.; Divitini, G.; Welland, M. E. Core−Shell Electrospun Polycrystalline ZnO Nanofibers for Ultra-Sensitive NO 2 Gas Sensing. *ACS Appl. Mater. Interfaces* **2018**, *10* (50), 43817−43823.
(47) Almenningen, A.; Halvorsen, S.; Haaland, A.; Pihlaja, K.; Schaumburg, K.; Ehrenberg, L. A Gas Phase Electron Diffraction Investigation of the Molecular Structures of Trimethylaluminium Monomer and Dimer. *Acta Chem. Scand.* **1971**, *25*, 1937−1945.
(48) Nam, C.-Y.; Stein, A.; Kisslinger, K. Direct Fabrication of High Aspect-Ratio Metal Oxide Nanopatterns via Sequential Infiltration Synthesis in Lithographically Defined SU-8 Templates. *J. Vac. Sci. Technol. B, Nanotechnol. Microelectron. Mater. Process. Meas. Phenom.* **2015**, *33* (6), No. 06F201.
(49) Stammler, H.-G.; Blomeyer, S.; Berger, R. J. F.; Mitzel, N. W. Trimethylaluminum: Bonding by Charge and Current Topology. *Angew. Chemie Int. Ed.* **2015**, *54* (46), 13816−13820.
(50) Negureanu, L.; Hall, R. W.; Butler, L. G.; Simeral, L. A. Methyaluminoxane (MAO) Polymerization Mechanism and Kinetic Model from Ab Initio Molecular Dynamics and Electronic Structure Calculations. *J. Am. Chem. Soc.* **2006**, *128* (51), 16816−16826.
(51) Hemraj-Benny, T.; Banerjee, S.; Sambasivan, S.; Balasubramanian, M.; Fischer, D. A.; Eres, G.; Puretzky, A. A.; Geohegan, D. B.; Lowndes, D. H.; Han, W.; Misewich, J. A.; Wong, S. S. Near-Edge X-Ray Absorption Fine Structure Spectroscopy as a Tool for Investigating Nanomaterials. *Small* **2006**, *2* (1), 26−35.
(52) Fallica, R.; Watts, B.; Rösner, B.; Della Giustina, G.; Brigo, L.; Brusatin, G.; Ekinci, Y. Changes in the near Edge X-Ray Absorption Fine Structure of Hybrid Organic−Inorganic Resists upon Exposure. *Nanotechnology* **2018**, *29* (36), 36LT03.
(53) Wu, L.; Bespalov, I.; Witte, K.; Lugier, O.; Haitjema, J.; Vockenhuber, M.; Ekinci, Y.; Watts, B.; Brouwer, A. M.; Castellanos, S. Unravelling the Effect of Fluorinated Ligands in Hybrid EUV Photoresists by X-Ray Spectroscopy. *J. Mater. Chem. C* **2020**, *8* (42), 14757−14765.

https://doi.org/10.1021/acs.chemmater.5c02584
Chem. Mater. 2026, 38, 1751−1765

(54) Wang, J.; Stöver, H. D. H.; Hitchcock, A. P.; Tyliszczak, T. Chemically Selective Soft X-Ray Patterning of Polymers. *J. Synchrotron Radiat.* **2007**, *14* (2), 181−190.
(55) Ju, H.; Feng, X.; Ye, Y.; Zhang, L.; Pan, H.; Campbell, C. T.; Zhu, J. Ca Carboxylate Formation at the Calcium/Poly(Methyl Methacrylate) Interface. *J. Phys. Chem. C* **2012**, *116* (38), 20465−20471.
(56) Thakur, P.; Bisogni, V.; Cezar, J. C.; Brookes, N. B.; Ghiringhelli, G.; Gautam, S.; Chae, K. H.; Subramanian, M.; Jayavel, R.; Asokan, K. Electronic Structure of Cu-Doped ZnO Thin Films by x-Ray Absorption, Magnetic Circular Dichroism, and Resonant Inelastic x-Ray Scattering. *J. Appl. Phys.* **2010**, *107* (10), 103915.
(57) Singh, A. P.; Kumar, R.; Thakur, P.; Brookes, N. B.; Chae, K. H.; Choi, W. K. NEXAFS and XMCD Studies of Single-Phase Co Doped ZnO Thin Films. *J. Phys.: Condens. Matter* **2009**, *21* (18), 185005.
(58) Alves, M. C. M.; Tourillon, G. Influence of Complexation Processes on the Catalytic Properties of Some Polymer-Based Cobalt Compounds for Oxygen Electroreduction. *J. Phys. Chem.* **1996**, *100* (18), 7566−7572.
(59) Hohenberg, P.; Kohn, W. Inhomogeneous Electron Gas. *Phys. Rev.* **1964**, *136* (3B), B864−B871.
(60) Rehr, J. J.; Albers, R. C. Theoretical Approaches to X-Ray Absorption Fine Structure. *Rev. Mod. Phys.* **2000**, *72* (3), 621−654.
(61) Rehr, J. J.; Kas, J. J.; Vila, F. D.; Prange, M. P.; Jorissen, K. Parameter-Free Calculations of X-Ray Spectra with FEFF9. *Phys. Chem. Chem. Phys.* **2010**, *12* (21), 5503.
(62) Grohens, Y.; Carriere, P.; Spevacek, J.; Schultz, J. Conformation of Stereoregular PMMA in Solutions during the Temperature Induced Conformational Transition. *Polymer (Guildf).* **1999**, *40* (25), 7033−7043.
(63) Iorio, M.; Teno, J.; Nicolás, M.; García-González, R.; Peláez, V. H.; González-Gaitano, G.; González-Benito, J. Conformational Changes on PMMA Induced by the Presence of TiO2 Nanoparticles and the Processing by Solution Blow Spinning. *Colloid Polym. Sci.* **2018**, *296* (3), 461−469.
(64) Ye, X.; Kestell, J.; Kisslinger, K.; Liu, M.; Grubbs, R. B.; Boscoboinik, J. A.; Nam, C.-Y. Effects of Residual Solvent Molecules Facilitating the Infiltration Synthesis of ZnO in a Nonreactive Polymer. *Chem. Mater.* **2017**, *29* (10), 4535−4545.
(65) Kestell, J. D.; Mudiyanselage, K.; Ye, X.; Nam, C.-Y.; Stacchiola, D.; Sadowski, J.; Boscoboinik, J. A. Stand-Alone Polarization-Modulation Infrared Reflection Absorption Spectroscopy Instrument Optimized for the Study of Catalytic Processes at Elevated Pressures. *Rev. Sci. Instrum.* **2017**, *88* (10), 105109.
(66) Goldstein, D. N.; McCormick, J. A.; George, S. M. Al_2O_3 Atomic Layer Deposition with Trimethylaluminum and Ozone Studied by in Situ Transmission FTIR Spectroscopy and Quadrupole Mass Spectrometry. *J. Phys. Chem. C* **2008**, *112* (49), 19530−19539.
(67) Balogun, S. A.; Yim, S. S.; Yom, T.; Jean, B. C.; Losego, M. D. Dealkylation of Poly(Methyl Methacrylate) by $TiCl_4$ Vapor Phase Infiltration (VPI) and the Resulting Chemical and Thermophysical Properties of the Hybrid Material. *Chem. Mater.* **2024**, *36* (2), 838−847.
(68) Grimme, S.; Brandenburg, J. G.; Bannwarth, C.; Hansen, A. Consistent Structures and Interactions by Density Functional Theory with Small Atomic Orbital Basis Sets. *J. Chem. Phys.* **2015**, *143* (5), No. 054107.
(69) Ghosh, B.; Ray, S. C.; Pontsho, M.; Sarma, S.; Mishra, D. K.; Wang, Y. F.; Pong, W. F.; Strydom, A. M. Defect Induced Room Temperature Ferromagnetism in Single Crystal, Poly-Crystal, and Nanorod ZnO: A Comparative Study. *J. Appl. Phys.* **2018**, *123* (16), 161507.
(70) Ozkendir, O. M.; Yildirimcan, S.; Yuzer, A.; Ocakoglu, K. Crystal and Electronic Structure Study of Mn Doped Wurtzite ZnO Nanoparticles. *Prog. Nat. Sci. Mater. Int.* **2016**, *26* (4), 347−353.
(71) Weiland, C.; Jaye, C.; Quackenbush, N. F.; Gann, E.; Fu, Z.; Kirkland, J. P.; Karlin, B. A.; Ravel, B.; Woicik, J. C.; Fischer, D. A. NIST HAXPES at NSLS and NSLS-II. *Synchrotron Radiat. News* **2018**, *31* (4), 23−28.
(72) Gann, E.; Crofts, T.; Holland, G.; Beaucage, P.; McAfee, T.; Kline, R. J.; Collins, B. A.; McNeill, C. R.; Fischer, D. A.; DeLongchamp, D. M. A NIST Facility for Resonant Soft X-Ray Scattering Measuring Nano-Scale Soft Matter Structure at NSLS-II. *J. Phys.: Condens. Matter* **2021**, *33* (16), 164001.
(73) Gann, E.; McNeill, C. R.; Tadich, A.; Cowie, B. C. C.; Thomsen, L. Quick AS NEXAFS Tool (QANT): A Program for NEXAFS Loading and Analysis Developed at the Australian Synchrotron. *J. Synchrotron Radiat.* **2016**, *23* (1), 374−380.
(74) Mardirossian, N.; Head-Gordon, M. ω B97M-V: A Combinatorially Optimized, Range-Separated Hybrid, Meta-GGA Density Functional with VV10 Nonlocal Correlation. *J. Chem. Phys.* **2016**, *144* (21), 214110.
(75) Liang, J.; Feng, X.; Liu, X.; Head-Gordon, M. Analytical Harmonic Vibrational Frequencies with VV10-Containing Density Functionals: Theory, Efficient Implementation, and Benchmark Assessments. *J. Chem. Phys.* **2023**, *158* (20), 204109.

https://doi.org/10.1021/acs.chemmater.5c02584
Chem. Mater. 2026, 38, 1751−1765